



UNIVERSITÀ POLITECNICA DELLE MARCHE
Repository ISTITUZIONALE

Unveiling the mono-rhamnolipid and di-rhamnolipid mechanisms of action upon plasma membrane models

This is the peer reviewed version of the following article:

Original

Unveiling the mono-rhamnolipid and di-rhamnolipid mechanisms of action upon plasma membrane models / Marega Motta, A.; Donato, M.; Mobbili, G.; Mariani, P.; Itri, R.; Spinozzi, F.. - In: JOURNAL OF COLLOID AND INTERFACE SCIENCE. - ISSN 0021-9797. - STAMPA. - 624:(2022), pp. 579-592. [10.1016/j.jcis.2022.05.145]

Availability:

This version is available at: 11566/308002 since: 2024-04-06T13:03:33Z

Publisher:

Published

DOI:10.1016/j.jcis.2022.05.145

Terms of use:

The terms and conditions for the reuse of this version of the manuscript are specified in the publishing policy. The use of copyrighted works requires the consent of the rights' holder (author or publisher). Works made available under a Creative Commons license or a Publisher's custom-made license can be used according to the terms and conditions contained therein. See editor's website for further information and terms and conditions.

This item was downloaded from IRIS Università Politecnica delle Marche (<https://iris.univpm.it>). When citing, please refer to the published version.

(Article begins on next page)

Unveiling the mono-rhamnolipid and di-rhamnolipid mechanisms of action upon plasma membrane models

Alessandra Marega Motta^a, Maressa Donato^b, Giovanna Mobbili^a, Paolo Mariani^a, Rosangela Itri^b, Francesco Spinozzi^{a,*}

^a*Department of Life and Environmental Sciences, Polytechnic University of Marche, Italy*

^b*Institute of Physics, University of São Paulo, Brazil*

Abstract

Rhamnolipids (RLs) are biosurfactants with significant tensioactive and emulsifying properties. They are mainly composed by mono-RL and di-RL components. Although there are numerous studies concerning their molecular properties, information is scarce regarding the mechanisms by which each of the two components interacts with cell membranes. Herein, we performed phase-contrast and fluorescence microscopy experiments on plasma membrane models represented by giant-unilamellar-vesicles (GUVs) composed of 1,2-dioleoyl-*sn*-glycero-3-phosphocholine (DOPC), 2-[[*(E,2S,3R)*-1,3-dihydroxy-2-(octadecanoylamino)octadec-4-enyl]peroxy-hydroxy-phosphoryl]oxyethyl-trimethylazanium (sphingomyelin, SM) and (3 β)-cholest-5-en-3-ol (cholesterol, CHOL) (1:1:1 molar ratio), which present liquid-order (L_o) liquid-disorder (L_d) phase coexistence, in the presence of either mono-RL or di-RL in 0.06-0.25 mM concentration range. A new method has been developed to determine area and volume of GUVs with asymmetrical shape and a kinetic model describing GUV-RL interaction in terms of two mechanisms, RL-insertion and pore formation, has been worked out. Results show that the insertion of mono-RL in the membrane outer leaflet is the dominant process with no pore formation and a negligible effect in modifying membrane permeability, but induces lipid mixing. Conversely, the di-RL-GUV interaction begins with the insertion mechanism and, as the time passes by, the pore formation process occurs. The analyses of di-RL show that the whole process is only relevant in the L_d phase with a higher extent to 0.25 mM than to 0.06 mM.

Keywords: membrane remodeling; lipid rafts; giant unilamellar vesicles; rhamnolipid; biosurfactant;

*Corresponding author

Email address: f.spinozzi@univpm.it (Francesco Spinozzi)

membrane protrusion.

1. Introduction

The search for new environmental technologies includes bioremediation, which aims to exploit microbial processes to biodegrade contaminants into less toxic compounds [1]. Among bioremediation processes, there are promising methodologies that make use of biosurfactants, a class of substances produced by microorganisms that control the biochemical and biophysical properties of their surface, for example by regulating the availability of water-insoluble molecules or by modulating their adhesion properties [2]. In this context, it has been reported that different strains of *Pseudomonas aeruginosa* are able to produce a class of biosurfactants called rhamnolipids (RL), with significant tensioactive and emulsifying properties that, among different applications, are able to enhance oil biodegradation, particularly relevant in soil/sand bioremediation processes [3]. The important application potentials of rhamnolipids have motivated the growing research activity aimed at characterizing their biochemical and structural properties [3].

From a molecular point of view, rhamnolipids are glycolipid surfactants with a hydrophilic head, composed of one or two molecules of rhamnose, connected to a hydrophobic tail, formed by one or two molecules of β -hydroxydecanoic acid. The most common forms and major components are L-rhamnosyl-L-rhamnosyl- β -hydroxydecanoyl- β -hydroxydecanoate ($\text{Rha}_2\text{C}_{10}\text{C}_{10}$) and L-rhamnosyl- β -hydroxydecanoyl- β -hydroxydecanoate ($\text{RhaC}_{10}\text{C}_{10}$), simply referred to as di-rhamnolipids (di-RL) and mono-rhamnolipids (mono-RL), respectively [4]. A variety of minor components of different alkyl chain length combinations, depending on the carbon source and bacterial strain, has been also reported [4]. Rhamnolipids in water behave as self-assembling molecules, able to aggregate and form micelles when they reach a concentration above the CMC (Critical Micelle Concentration). This characteristic gives them the capacity of increasing solubilization of organic compounds, for example hydrocarbons from petroleum, by dissolving the compounds and keeping them inside the hydrophobic core of the micelles [5]. It has been shown that at high concentration, above CMC, mono-RLs self-associate into predominantly planar structures (lamellar or unilamellar/bilamellar vesicles) whereas di-RLs remain in the form globular micelles [4]. Hence, rhamnolipids mixtures rich in di-RL are predominantly micellar and those rich in mono-RL have mostly planar structures. At intermediate mono-RL/di-RL compositions, lamellar/micellar

coexistence exists, but the higher curvature associated with di-RL dominates the mono-RL/di-RL mixing behavior [4]. The CMC of pure rhamnolipids and its mixtures depends on the chemical composition of the various species and it ranges from 0.1 to 0.4 mM [6].

In general, bacteria produce a heterogeneous mixture of biosurfactants. It is therefore important to evaluate the specific physicochemical and biological features of each component of the mixture in order to identify which are the components with the molecular properties suitable for optimized technological uses [7]. In the case of rhamnolipids produced by *P. aeruginosa*, as they constitute a mixture of mono-RL and di-RL, it is necessary to investigate not only the physicochemical and biological properties of the mixture, but also the ones corresponding to each component [3]. Despite a number of studies already performed, little is known about the molecular basis of some biological actions of rhamnolipids, like permeabilization and membrane rupture, which are important for biocide action. Also, for pharmaceutical, cosmetic as well as environmental purposes, it is important to correlate rhamnolipids action mechanisms on biological membranes with their molecular structures [8].

The complexity of cellular membranes in composition and dynamic organization has motivated the development of a variety of simpler model systems that serve as a test for investigating more complex biological membranes. In this framework, giant unilamellar vesicles (GUVs) are simple model membrane systems of cell-size, which allows us to study the behavior of more complex biological membranes, involving heterogeneities in lipid composition, shape, mechanical and chemical properties [9]. The GUVs dimensions (1-100 microns) and their curvature enable one to visualize them individually using optical microscopy [10]. The lipid composition of GUVs may change from a single lipid component to a mixture of lipids [11]. Performing experiments with GUVs being exposed to mono-RL and di-RL allows investigating the interaction of these biosurfactants with lipid bilayers to understand their impact on plasma membrane at molecular level. In this context, recently some of us studied the interactions of a commercial mixture of rhamnolipids with plasma membrane models represented by GUVs [8]. Results indicated that rhamnolipids, at concentrations from 0.1 to 0.5 mM, are able to promote membrane remodeling, with no lytic effect. In GUVs formed by POPC (2-oleoyl-1-palmitoyl-*sn*-glycero-3-phosphocholine), the insertion of the rhamnolipids mixture promotes an increase of the vesicle area, followed by a release of the excess area through the formation of small buds. The commercial RLs mixture in contact with GUVs formed by DOPC (1,2-dioleoyl-

sn-glycero-3-phosphocholine), SM (sphingomyelin, 2-[[*(E,2S,3R)*-1,3-dihydroxy-2-(octadecanoylamino)octadec-4-enyl]peroxy-hydroxyphosphoryl]oxyethyl-trimethylazanium) and CHOL (cholesterol, (3 β)-cholest-5-en-3-ol) at molar ratio 1:1:1, which showed a clear liquid ordered - liquid disordered (L_d - L_o) phase separation, promoted budding on a micro-scale in the L_o phase. The analysis of optical contrast microscopy snapshots revealed that RLs insert preferentially in the L_d phase. The interaction of surfactant molecules with lipid membranes is central to many processes across the plant and animal kingdom. One of the fundamental features of surfactant-membrane interactions is that the surfactants can insert themselves within the lipid bilayer and alter the surface area of the membrane through lipid solubilization [12]. The classical model describing the behavior of the surfactant-lipid systems as a function of the surfactant's relative concentration is the three-stage model proposed by Helenius and Simons [13]: first, at low surfactant concentration, the surfactant molecules partition into the membrane; second, above a critical surfactant concentration, membrane solubilization occurs and mixed micelles coexist with the lipid membrane, and finally, above a second critical surfactant concentration, only micelles remain [12]. Water enters in living membranes through both the lipid bilayer and through specific water transport proteins and in both cases water flow is directed by osmosis. The rate through the lipid bilayer depends on lipid structures and the presence of sterols [14]. Previous studies treated water diffusion through lipid bilayers as solubility-diffusion. Given the entropic energy that maintains the intrinsic oil-water interface, it is surprising that water passes so easily through bilayers [14]. Deamer and Bramhall [15] proposed a defect model in which the lipids of the bilayer molecules (only two molecules thick) are separated just enough at some discrete frequency allowing water to pass through the membrane.

The current work aims to gather new information in respect to the previous work [8] regarding the role of mono-RL and di-RL individually on model lipid bilayers representing plasma membranes. To this aim, we performed phase contrast and fluorescence microscopy experiments on dispersions of GUVs in the presence of either mono-RL or di-RL, at different concentrations. The two forms of RLs have been separated from the commercial mixture using a column chromatography. We investigated ternary GUVs formed of DOPC, sphingomyelin (SM) and cholesterol (CHOL) at molar ratio 1:1:1. A new method to analyse the microscope images of GUVs with asymmetrical shapes has been developed, allowing the determination of their area and volume. Moreover, we have analyzed the GUVs area and volume with a new kinetic model that describes the

GUV-RL interaction in terms of both RL-insertion, with possible modification of membrane permeability, and pore formation. Results allow us to quantify the distinct behaviors of mono-RL and di-RL in model plasma membrane remodeling.

2. Material and methods

2.1. Rhamnolipids separation

Rhamnolipid from *Pseudomonas aeruginosa* (in powder and purity of 90%) was purchased from Sigma-Aldrich (Poole, UK). This commercial product was described by Perinelli et al [16] and is composed of a mixture of mono-RL (33-37 mol%) and di-RL (63-67 mol%). The CMC in water was estimated as 0.16 mM. The separation of mono-RL and di-RL from the rhamnolipids mixture was carried out using column chromatography as described by Ortiz et al [17]. Briefly, silicagel 60 in chloroform (Sigma-Aldrich, purity > 99%) was poured onto a glass chromatography column (2×40 cm). Then 2.0 g of the crude rhamnolipid mixture was dissolved in 4 mL of chloroform and loaded into the column. The column was washed with chloroform until neutral lipids were totally eluted, followed by chloroform/methanol 50:3 and 50:5 (methanol from Sigma-Aldrich, purity > 99.5%), which extract the mono-rhamnolipid component, and chloroform/methanol 50:50 and pure methanol, which extract the di-rhamnolipid component. The composition of the fractions was checked by thin-layer chromatography on silica gel plates using chloroform/methanol (9:1) as mobile phase. The purified mono and di-rhamnolipids components were quantified by weight after desiccation under high vacuum. The chemical characterization of the compounds was confirmed by electrospray mass spectroscopy as previously described [17] (Fig. S1 of SI). The sample containing mono-rhamnolipids was mainly composed of molecules with molecular weight of 502 Da, whereas most of the molecules in the di-rhamnolipids sample showed a molecular weight of 648 Da. According to the literature, these molecular weights can be attributed to mono-rhamnolipids Rha-C₁₀-C₁₀ and di-rhamnolipids Rha-Rha-C₁₀-C₁₀, respectively [18].

2.2. CMC determination

The determination of the CMC of mono-RL and di-RL was performed via surface tension measurements, using a Langmuir equipment. A home-built round teflon trough (diameter 20 mm, depth 2 mm) filled with 1200 μ L of RL solutions was used for the experiments [19]. A stock solution of mono-RL and di-RL was prepared

and then diluted to obtain different concentrations, from 0.0005 to 0.8 mM. Experiments were realized in both water and 0.2 M glucose (Sigma-Aldrich, purity > 99.5%), the same concentration used in the GUV experiments, see later. The experiments were done in triplicate and the data correspond to the average surface tension value at each biosurfactant concentration. The uncertainties take into account the maximum and minimum values obtained. The CMC was determined from the break-point observed in the plot of the surface tension *vs.* log surfactant concentration. It should be stressed that the CMC value in the presence of a membrane is unknown, since we do not know *a priori* the partition of both biosurfactants towards the lipid membrane in respect to the solution. This will be addressed through the kinetic model used ahead in the text (Section 2.6). For this reason, GUVs experiments were carried out with the same mono-RL and di-RL molar concentrations, regardless its individual CMC in glucose.

2.3. GUV preparation

GUVs were prepared by employing the following lipid molecules: DOPC (1,2-dioleoyl-*sn*-glycero-3-phosphocholine, from Avanti Polar Lipids, purity > 99%), sphingomyelin (SM, 2-[[*(E,2S,3R)*-1,3-dihydroxy-2-(octadecanoylamino)octadec-4-enyl]peroxy-hydroxyphosphoryl]oxyethyl-trimethylazanium, from Avanti Polar Lipids, purity > 99%), cholesterol (CHOL, 3 β -hydroxy-5-cholestene, from Avanti Polar Lipids, purity > 99%) and DOPE (1,2-dioleoyl-*sn*-glycero-3-phosphoethanolamine, from Avanti Polar Lipids, purity > 99%)-rhodamine (from Avanti Polar Lipids, purity > 99%) (Rho-PE). All other chemicals and solvents were purchased from Sigma-Aldrich (Saint Louis, MO) and used without further purification. GUVs were prepared by electroformation procedure [8] using a combination of DOPC, SM, CHOL (molar ratio 1:1:1), containing the fluorescence probe Rho-PE (0.1 mol %). First, 20 μ L of 1.0 g/L total lipid in chloroform solution were spread on the surfaces of two conductive glass slides coated with indium tin oxide (ITO slides, Sigma-Aldrich, Saint Louis, MO), placed with their conductive sides fronting each other and separated by a 2 mm thick Teflon frame, forming a chamber. This was filled with a 0.2 M sucrose (Sigma-Aldrich, purity > 99.5%) solution, with a volume of 1.0 mL, and the glass plates were connected to a voltage generator for 2 h (2 V with 10 Hz frequency). The electroformation of GUVs composed of DOPC:SM:CHOL was conducted at 55° C and then these GUVs were left at 4° C overnight and observed the following day. Thereafter, 100 mL of electroformed GUVs were mixed to 600 mL of a 0.2 M glucose solution containing mono-RL or di-RL and immediately transferred to the microscope chamber to perform continuous

observations. The osmolarities of sucrose and glucose solutions were measured with a cryoscopic osmometer Osmomat 030 (Gonotec, Germany) and carefully matched to avoid osmotic pressure effects to guarantee the optical contrast. The final total lipid w/v concentration was 0.00286 g/L while the molar concentrations of either mono-RL or di-RL were 0.06 mM, 0.12 mM and 0.25 mM. For each of the 6 experimental conditions (3 for mono-RL and 3 for di-RL), with the exception of the one with 0.25 mM di-RL, the experiments were repeated three times..

2.4. Microscope observations

GUVs were observed in the phase contrast and fluorescence modes by means of an inverted microscope Axiovert 200 (Carl Zeiss, Jena, Germany) equipped with a Plan Neo-Fluar 63x Ph2 objective (NA 0.75). Images were recorded with an AxioCam HSm digital camera (Carl Zeiss). A mercury lamp HBO 103 W, with excitation and emission filters at 540-552 nm and 575-640 nm in fluorescence mode, was used. The effect of lipid oxidation was controlled by a low intensity illumination in the fluorescence microscopy to avoid artifacts due to light-induced domain formation by the Rho-probe [20, 21]. All measurements were performed at $(23 \pm 1)^\circ \text{C}$. After mixing glucose with GUVs and different concentrations of either mono-RL or di-RL, the observation of vesicles were realized for nearly 20 min, taking one snapshot each second, hence totalizing 1200 images for each experiment. To analyse the images taken from the microscope observations, we choose about 120 snapshots from each of the 6 experimental conditions, selecting the images with a 10 s interval. They are reported in SI: Figs. S6, S10 and S15 (three experiments with 0.06 mM mono-RL), Figs. S7, S11 and S16 (three experiments with 0.12 mM mono-RL), Figs. S8, S12 and S17 (three experiments with 0.25 mM mono-RL), Figs. S20, S24 and S28 (three experiments with 0.06 mM di-RL), Figs. S21, S25 and S29 (three experiments with 0.12 mM di-RL) and Fig. S22 (one experiment with 0.25 di-RL).

2.5. Microscope data analysis of asymmetrical GUVs images

The images collected for each sample of GUVs prepared with a given lipid composition, as function of the time elapsed after the mixing with a solution of either mono-RL or di-RL at a given concentration, were analyzed using a novel method that has been implemented through a series of macros under the **ImageJ** software [22]. We first developed a method for determining the surface area and volume of distorted or fluctuating circle-shaped GUV that does not show phase separation (homogeneous GUV). A second method was developed for

detecting the shape of a GUV that undergoes a phase separation process, clearly visible under fluorescence mode microscope observations. These GUVs, in general, are formed by two phases, whose edges, on average, follow the profile of two distinct arcs of circumference, which, in some cases, can show fluctuations. Let us assume that the users has manually selected a series of $\{x_i, y_i\}$ points (pixel coordinates saved under **ImageJ**) around the border of a homogeneous GUV or around each of the two borders of a two-phase-domain GUV. The purpose of the new method is to find the best smooth contour the passes among these points. To this aim, we assume that the border of the GUV phase around its centre position x_c, y_c can be described by a positive function $r(\theta)$, in polar coordinates, giving the distance of the border from the centre as a function of the angle θ formed by the radial direction with the x axis (Fig. 1, panel A). Clearly, this function must have a 2π periodicity, hence it is well suited to be expanded in Fourier series,

$$r(\theta) = R \left[1 + \sum_{k=1}^{N_F} a_k \sin(k\theta) + b_k \cos(k\theta) \right] \quad (1)$$

where R is the average radius, N_F is the maximum order of the Fourier expansion and the dimensionless parameters a_k and b_k are the sine and cosine expansion coefficients, according to

$$R = \int_0^{2\pi} r(\theta) d\theta \quad (2)$$

$$a_k = \frac{1}{R} \int_0^{2\pi} r(\theta) \sin(k\theta) d\theta \quad (3)$$

$$b_k = \frac{1}{R} \int_0^{2\pi} r(\theta) \cos(k\theta) d\theta \quad (4)$$

Hence the position and the 2D shape of the GUV domain is mapped in a set of $m = 3 + 2N_F$ parameters: $x_c, y_c, R, \{a_k, b_k\}$. The optimum values of these parameters are obtained by numerical minimization of the

following merit function

$$H = \sum_i (x_i - x_{\text{fit},i})^2 + (y_i - y_{\text{fit},i})^2 + \alpha_F \sum_k a_k^2 + b_k^2 \quad (5)$$

$$x_{\text{fit},i} = x_c + r_{\text{fit}}(\theta_i) \cos(\theta_i) \quad (6)$$

$$y_{\text{fit},i} = y_c + r_{\text{fit}}(\theta_i) \sin(\theta_i) \quad (7)$$

$$\theta_i = \text{atan2}(y_i - y_c, x_i - x_c) \quad (8)$$

where $\text{atan2}(y, x)$ is the 2-argument arctangent function [23]. Notice that H is the sum between two terms: the squared distance between observed and fitted points and a “regularization” term that avoids large values of a_k and b_k , leading to over-sized fluctuations. The relative weight between the two terms is ruled by the α_F parameter that was fixed in order that, at the end of the fit, the regularization term accounts for approximately 10% the first one. By repeating several times the H minimization and, for each minimization, by sampling the points’ coordinates within a 2D Gaussian centered in $\{x_i, y_i\}$ with fixed standard deviation σ (we have chosen $\sigma = 2 \mu\text{m}$), we can estimate the standard deviations of all fitting parameters. Some tests of the validity of this method are reported in SI, Fig. S2.

Concerning homogeneous GUVs, the area and the volume are calculated on the basis of $r(\theta)$ by considering the revolution solid generated by a rotation of 2π around the x axis. Since in some circumstances the GUV border can be elongated, in order to avoid an over-estimation of both area and volume of the GUV, before to generate the solid of revolution, the function $r(\theta)$ is rotated around the z axis by the angle $-\theta_0$, θ_0 being the angle formed by the direction of the maximum diameter with the axis x , according to $d = \{r(\theta_0) + r(\pi + \theta_0)\}_{\text{max}}$ (Fig. 1, panels A and B). On this basis, the homogeneous GUV area and volume are obtained by the well-known expressions of the differential calculus for polar functions,

$$A = \pi \int_0^{2\pi} r(\theta + \theta_0) |\sin \theta| \sqrt{r^2(\theta + \theta_0) + \left(\frac{dr(\theta)}{d\theta}\right)^2} d\theta \quad (9)$$

$$V = \frac{\pi}{3} \int_0^{2\pi} r^3(\theta + \theta_0) |\sin \theta| d\theta \quad (10)$$

Notice that, since, in general, $r(\theta)$ is asymmetric, when the border is rotated by 2π around x , two different

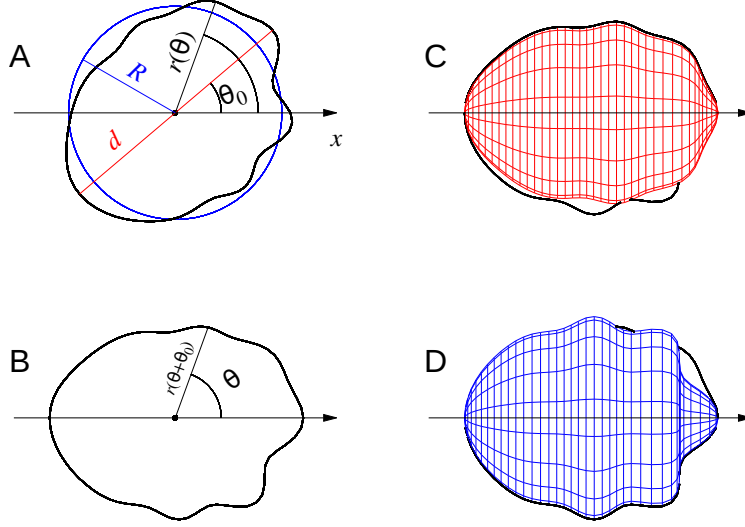


Figure 1: Representation of a homogeneous fluctuating GUV.

solids of revolution are generated (Fig. 1, panels C and D). Anyhow, it should be remarked that the upper integration bound 2π seen in both Eqs. 9 and 10 ensures a correct determination of the average area and the average volume of the two solids of revolution.

We turn now to the case of GUVs that present phase coexistence (two-phase-domain GUVs). The selection by the user of two sets of points $\{x_i, y_i\}$ over the border of the two domains (L_d and L_o , shortly indexed by d and o), will allow to optimize the two corresponding functions $r_d(\theta)$ and $r_o(\theta)$ as well as the coordinates of their centers $x_{c,d}, y_{c,d}$ and $x_{c,o}, y_{c,o}$, which immediately allow to derive the centers' distance, $r_{do} = \sqrt{(x_{c,o} - x_{c,d})^2 + (y_{c,o} - y_{c,d})^2}$, and the angle θ_0 formed by the direction connecting the two centers with the x axis, $\theta_0 = \text{atan2}(y_{c,o} - y_{c,d}, x_{c,o} - x_{c,d})$ (Fig. 2, panel A). The two lipid domains are not totally separated when there are two points of intersection between the functions that define the two corresponding borders. It can be easily demonstrated that this condition is verified when there are two pairs of real solutions $\theta_{d,j}, \theta_{o,j}$

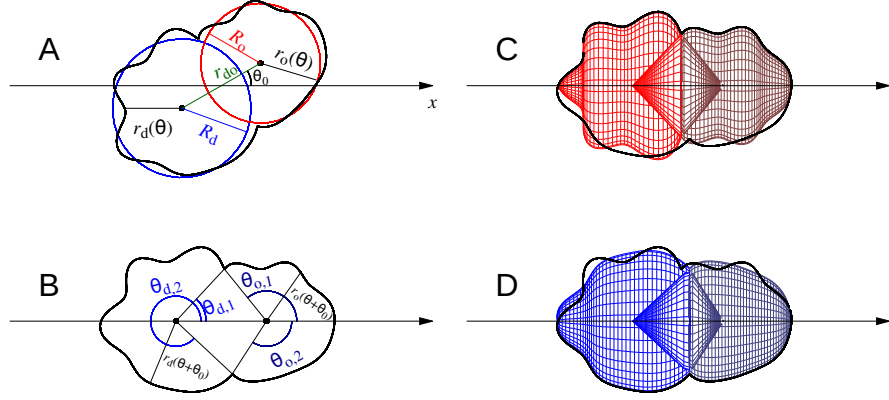


Figure 2: Representation of a two-phase-domain fluctuating GUV.

(with $j = 1, 2$) of the following equation (Fig. 2, panel B)

$$\begin{aligned}
 & [r_{do} + r_o(\theta_{o,j} + \theta_0) \cos(\theta_{o,j}) - r_d(\theta_{d,j} + \theta_0) \cos(\theta_{d,j})]^2 \\
 & + [r_o(\theta_{o,j} + \theta_0) \sin(\theta_{o,j}) - r_d(\theta_{d,j} + \theta_0) \sin(\theta_{d,j})]^2 = 0
 \end{aligned} \tag{11}$$

In the example of Fig. 2, panel B, the four angles $\theta_{k,j}$ are indicated. If there are not real solutions of Eq. 11, the two domains are totally separated and we take $\theta_{d,1} = \theta_{o,1} = 0$ and $\theta_{d,2} = \theta_{o,2} = 2\pi$. Under these conditions, the area of the α -phase ($\alpha = d, o$) is

$$A_\alpha = \pi \int_{\theta_{\alpha,1}}^{\theta_{\alpha,2}} r_\alpha(\theta + \theta_0) |\sin \theta| \sqrt{r_\alpha^2(\theta + \theta_0) + \left(\frac{dr_\alpha(\theta)}{d\theta} \right)^2} d\theta \tag{12}$$

To note, this area corresponds to the average to the areas of the two revolution solids shown in Fig. 2, panels C and D, which are related to the rotation around the x axis of the function $r_\alpha(\theta + \theta_0)$ (for $\alpha = d$ the two solids are shown in red (panel C) and blue (panel D), respectively; for $\alpha = o$ they are shown in dark-red (panel C) and dark-blue (panel D), respectively). The corresponding volumes are calculated by the integral

with bounds $\theta_{\alpha,1}, \theta_{\alpha,2}$, to which the average of volumes of the two cones with radius $r_{\alpha}(\theta_{\alpha,j} + \theta_0) \sin \theta_{\alpha,j}$ and height $r_{\alpha}(\theta_{\alpha,j} + \theta_0) |\cos \theta_{\alpha,j}|$ (represented in Fig. 2, panels C and D, in red and dark-red for $\alpha = d$ and in blue and dark-blue for $\alpha = o$) should be added. Accordingly, we obtain

$$V_{\alpha} = \frac{\pi}{3} \left[\frac{1}{2} \sum_{j=1}^2 r_{\alpha}^3(\theta_{\alpha,j} + \theta_0) \sin^2 \theta_{\alpha,j} |\cos \theta_{\alpha,j}| + \int_{\theta_{\alpha,1}}^{\theta_{\alpha,2}} r_{\alpha}^3(\theta + \theta_0) |\sin \theta| d\theta \right] \quad (13)$$

The total area and the total volume of the solid of revolution representing the two-phase-domain GUV will clearly be $A = A_d + A_o$ and $V = V_d + V_o$, respectively.

2.6. Kinetic model of GUV:RL interaction

Let us now consider the specific GUV that is observed under the microscope as a function of the time t after the mixing with a solution of either mono-RL or di-RL. The time evolution of both the GUV area and the GUV volume, derived by the analysis of microscopy images according to Section 2.5, cannot be approximated by simple linear functions, suggesting more complex kinetic processes triggered by the presence of RLs. We also notice that, in some cases, the increase of the area is followed by a concomitant increase of the GUV volume, clearly indicating that a not negligible amount of solution has entered into the GUV. In other circumstances, similar to the ones observed by Come et al. [8] for commercial RL samples, the GUV volume remains almost constant, despite the increase of the area, showing that mono-RL and di-RL molecules mostly interact with the outer leaflet, with a small effect on the vesicle integrity. These observations apply to both homogeneous and two-phase-domain GUVs, in this latter case with distinct effects on L_d and L_o phases. On these bases, we have worked out a basic kinetic model that includes two approaches, for either homogeneous or two-phase-domain GUVs, and that turned out to be able to quantitatively catch the simple molecular mechanisms ruling the RL:GUV interactions.

2.6.1. Homogeneous GUVs

We assume that RL molecules interact with the *average lipid molecule* \mathbf{E} (according to the definitions introduced in Sect. S2 of SI) constituting the GUV with two equilibrium processes. The first process describes

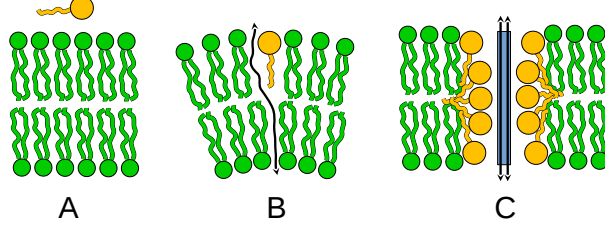


Figure 3: Representation of the interaction mechanisms between RLs (orange spheres) and GUVs (green lipids). A: RL-unbound GUV bilayer. B: a RL molecule bound to the outer leaflet of the GUV via the first mechanism referred to as *RL-insertion*. The black line is indicative of tortuous path through which the inner/outer solution exchange would occur due to possible RL-induced increase of the GUV permeability. C: aggregated RL molecules on the surface of a pore via the second mechanism referred to as *pore formation*. The black lines refers to the easy solution exchange through the pore, here represented by a cyan cylinder with radius r_p and height t_b .

the embedding of free RLs in solution into the outer leaflet of the vesicle, with an increase of the GUV area and a possible increase of the GUV volume, an event that could occur when the inclusion of RLs increases the permeability of the lipid bilayer to the aqueous solution [14, 12]. We refer to this first process as *RL-insertion* (Fig. 3B). The second process is an aggregation among the RL molecules already present in the GUV vesicle. This aggregation is necessary for the formation of pores, which are stabilized by the disposal of aggregated RL molecules into the pores' internal surface [12]. In such a case, marked effects on both GUV area and volume are predictable. We call this second process as *pore formation* (Fig. 3C). The two processes are treated as two consecutive and reversible reactions, according to the following kinetic scheme



where m and n are the effective kinetic orders of the two processes. Direct and reverse kinetic constants of the first process are k_{1+} (in units of $\text{s}^{-1}\text{M}^{-m}$) and k_{1-} (in units of s^{-1}), whereas k_{2+} (in units of $\text{s}^{-1}\text{M}^{1-n}$) and k_{2-} (in units of s^{-1}) refer to the second process. As a result of the two consecutive processes, a fraction f_1 of RL will be dispersed into the GUV through RL-insertion and a fraction f_2 of RL will be involved in pore

formation. These fractions can be defined as follows

$$\begin{aligned} f_1 &= \frac{m[\text{RL}_m\mathbf{E}]}{C_{\text{RL}}} \\ f_2 &= \frac{mn[(\text{RL}_m\mathbf{E})_n]}{C_{\text{RL}}} \end{aligned} \quad (15)$$

where C_{RL} is the nominal concentration of RL (corresponding to the concentration of RL in glucose solution at $t = 0$, see Sect. S2 of SI). We also define the total fraction f of RL entered into the GUV, $f = f_1 + f_2$. It is easy to express the concentration of RL not bound to the GUV and the concentration of lipid molecule not interacting with RL molecules as follows, where C is the nominal concentration of lipids. With these definitions, the scheme 14 leads to the following system of differential equations,

$$\begin{cases} \frac{d}{dt}f_1 = F_1 - F_2 \\ \frac{d}{dt}f_2 = F_2 \end{cases} \quad (16)$$

where F_1 and F_2 are the following factors

$$\begin{aligned} F_1 &= k_{1+}C_{\text{RL}}^{m-1}(1-f)^m(mC - C_{\text{RL}}f) - k_{1-}f_1 \\ F_2 &= k_{2+}m^{1-n}nC_{\text{RL}}^{n-1}f_1^n - k_{2-}f_2 \end{aligned} \quad (17)$$

The solution of the system 16 can be performed with numerical methods and allows to derive the two time-functions $f_1(t)$ and $f_2(t)$. These functions are exploited to model the increase, as a function of time, of both GUV area and volume, as seen by the microscope observations. The GUV area at $t = 0$ is $A_0 = Na/2$, where N is the number of lipid molecules that form the GUV lipid bilayer and a is the average area per lipid polar head (see Sect. S2 and Table S1 in SI for details). The area increase due to the first process (RL-insertion) depends on the $f_1(t)$ fraction, according to $A_1(t) = Na_{\text{RL}}\zeta f_1(t)$, where a_{RL} is the average area of the RL polar head molecule, here considered to be constant, and ζ is the nominal RL-to-lipid molar ratio. Also the second process (pore formation) will contribute to the overall increase of the GUV area seen by the microscope observations. For the sake of simplicity, we assume that all pores have the same cylindrical shape, with average radius r_p and lateral area $2\pi r_p t_b$, t_b being the thickness of the bilayer. Each pore will contribute to increase the GUV

area by πr_p^2 and will involve an average number of RL molecules corresponding to $n_{\text{RL},p} = 2\pi r_p t_b / a_{\text{RL}}$. By these assumptions, the GUV area increase due to the pore formation process is $A_2(t) = N\zeta f_2(t)\pi r_p^2 / n_{\text{RL},p}$. In summary, the overall GUV area is modeled by the following equation

$$\begin{aligned} A(t) &= A_0 + A_1(t) + A_2(t) \\ &= N \left[\frac{a}{2} + a_{\text{RL}}\zeta \left(f_1(t) + \frac{r_p}{2t_b} f_2(t) \right) \right]. \end{aligned} \quad (18)$$

The time evolution of the GUV volume depends, in general, on the volume flux $J = \frac{1}{A} \frac{dV}{dt}$ of the water solution across the membrane, which, in turn, depends on various factors, including osmotic pressure, membrane elasticity, curvature, permeability and presence of pores as well as on their time variation. However, our experiments do not contain the information necessary to determine all these parameters. Under these conditions, we propose the simple hypothesis that the rate of increase of the GUV volume caused by the first process (RL-insertion) is directly proportional to the rate of increase of the GUV area relative to the same process, $\frac{dV_1(t)}{dt} \propto \frac{dA_1(t)}{dt}$, hence

$$V_1(t) = \lambda_1 N a_{\text{RL}} \zeta f_1(t), \quad (19)$$

where λ_1 is a constant with dimensions of a length. Likewise, we assume that the rate of GUV volume increase due to the second process (pore formation) is directly proportional to the corresponding rate of GUV area increase, $\frac{dV_2(t)}{dt} \propto \frac{dA_2(t)}{dt}$, so that

$$V_2(t) = \lambda_2 N a_{\text{RL}} \zeta \frac{r_p}{2t_b} f_2(t), \quad (20)$$

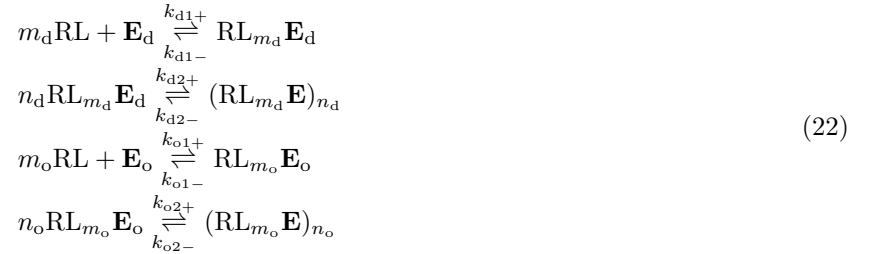
where a second constant, λ_2 , with dimensions of a length has been introduced. The GUV volume will be

$$\begin{aligned} V(t) &= V_0 + V_1(t) + V_2(t) \\ &= V_0 + N a_{\text{RL}} \zeta \left[\lambda_1 f_1(t) + \lambda_2 \frac{r_p}{2t_b} f_2(t) \right] \end{aligned} \quad (21)$$

The experimental values of A and V obtained by microscope observations as a function of the time after the mixing of GUV and RL solution can be simultaneously fitted with Eqs. 18 and 21. As a result all the kinetic parameters that rule the processes shown in scheme 14 can be derived. The uncertainty on these parameters is calculated by repeating the data analysis after having sampled, for each time value, the GUV area and volume from Gaussians having the standard deviation equal to the uncertainties of A and V determined by the ImageJ macro.

2.6.2. Two-phase-domain GUVs

In the case of GUVs formed by separated L_d and L_o phases, we can extend the previous kinetic model by considering the following four processes that involve RL molecules and both average disordered and average ordered lipid molecules (\mathbf{E}_d and \mathbf{E}_o , respectively, see Sect. S2 in SI for details),



where m_α and n_α are the kinetic orders of RL-insertion (with direct and reverse constants $k_{\alpha 1+}$ and $k_{\alpha 1-}$) and pore formation (with direct and reverse constants $k_{\alpha 2+}$ and $k_{\alpha 2-}$), respectively, occurring in the α -phase (with $\alpha = d, o$). The concentrations of all species involved in the four processes must obey mass balance constraints, according to

$$\begin{aligned}
C_d &= [\mathbf{E}_d] + [\text{RL}_{m_d} \mathbf{E}_d] + n_d [(\text{RL}_{m_d} \mathbf{E})_{n_d}] \\
C_o &= [\mathbf{E}_o] + [\text{RL}_{m_o} \mathbf{E}_o] + n_o [(\text{RL}_{m_o} \mathbf{E})_{n_o}] \\
C_{\text{RL}} &= [\text{RL}] + m_d [\text{RL}_{m_d} \mathbf{E}_d] + m_d n_d [(\text{RL}_{m_d} \mathbf{E})_{n_d}] \\
&\quad + m_o [\text{RL}_{m_o} \mathbf{E}_o] + m_o n_o [(\text{RL}_{m_o} \mathbf{E})_{n_o}].
\end{aligned} \tag{23}$$

We hence introduce the fractions of RL involved in *RL-insertion* or *pore formation* over both phases,

$$\begin{aligned}
f_{d,1} &= \frac{m_d[\text{RL}_{m_d}\mathbf{E}_d]}{C_{\text{RL}}} \\
f_{d,2} &= \frac{m_d n_d [(\text{RL}_{m_d}\mathbf{E})_{n_d}]}{C_{\text{RL}}} \\
f_{o,1} &= \frac{m_o[\text{RL}_{m_o}\mathbf{E}_o]}{C_{\text{RL}}} \\
f_{o,2} &= \frac{m_o n_o [(\text{RL}_{m_o}\mathbf{E})_{n_o}]}{C_{\text{RL}}}
\end{aligned} \tag{24}$$

To note, the total fractions of RL bound either to L_d or L_o phases are $f_d = f_{d,1} + f_{d,2}$ and $f_o = f_{o,1} + f_{o,2}$, respectively, whereas the fraction of RL bound to the the whole GUV is $f = f_d + f_o$. We can also derive the concentrations of free RL, lipid disordered and lipid ordered molecules, $[\text{RL}] = (1-f)C_{\text{RL}}$, $[\mathbf{E}_d] = C_d - \frac{1}{m_d}f_d C_{\text{RL}}$ and $[\mathbf{E}_o] = C_o - \frac{1}{m_o}f_o C_{\text{RL}}$. The system of four processes reported in the scheme 22 gives rise to the following system of differential equations,

$$\begin{cases} \frac{d}{dt}f_{d,1} = F_1 - F_2 \\ \frac{d}{dt}f_{d,2} = F_2 \\ \frac{d}{dt}f_{o,1} = F_3 - F_4 \\ \frac{d}{dt}f_{o,2} = F_4 \end{cases} \tag{25}$$

where F_j ($j = 1, 4$) are the following factors

$$\begin{aligned}
F_1 &= k_{d1+}(1-f)^{m_d}C_{\text{RL}}^{m_d-1}(m_d C_d - f_d C_{\text{RL}}) - k_{d1-}f_{d,1} \\
F_2 &= -k_{d2-}f_{d,2} + k_{d2+}m_d^{1-n_d}n_d f_{d,1}^{n_d}C_{\text{RL}}^{m_d-1} \\
F_3 &= k_{o1+}(1-f)^{m_o}C_{\text{RL}}^{m_o-1}(m_o C_o - f_o C_{\text{RL}}) - k_{o1-}f_{o,1} \\
F_4 &= -k_{o2-}f_{o,2} + k_{o2+}m_o^{1-n_o}n_o f_{o,1}^{n_o}C_{\text{RL}}^{m_o-1}
\end{aligned} \tag{26}$$

The system can be solved by numerical methods, allowing the simultaneous determination of the four functions $f_{d,1}(t)$, $f_{d,2}(t)$, $f_{o,1}(t)$ and $f_{o,2}(t)$. Then, on the basis of the same mechanisms invoked for the determination of the time dependency of the GUV area and volume of homogeneous GUVs (see Eqs. 18 and 21), we can easily

derive the area of the α -phase of the GUV,

$$\begin{aligned} A_\alpha(t) &= A_{\alpha,0} + A_{\alpha,1}(t) + A_{\alpha,2}(t) \\ &= N_\alpha \left[\frac{a_\alpha}{2} + a_{\text{RL}} \zeta_\alpha \left(f_{\alpha,1}(t) + \frac{r_{p,\alpha}}{2t_{b,\alpha}} f_{\alpha,2}(t) \right) \right] \end{aligned} \quad (27)$$

as well as the volume of the α -phase of the GUV

$$\begin{aligned} V_\alpha(t) &= V_{\alpha,0} + V_{\alpha,1}(t) + V_{\alpha,2}(t) \\ &= V_{\alpha,0} + N_\alpha a_{\text{RL}} \zeta_\alpha \left[\lambda_{\alpha,1} f_{\alpha,1}(t) + \lambda_{\alpha,2} \frac{r_{p,\alpha}}{2t_{b,\alpha}} f_{\alpha,2}(t) \right] \end{aligned} \quad (28)$$

where the parameters referring to the α -phase have the same meaning of the corresponding ones in Eqs. 18 and 21. It is worth to notice that the kinetic model for two-phase-domain GUV allows to fit by a unique calculation four experimental curves, corresponding to the areas and the volumes of both L_d and L_o GUV phases. The uncertainties on the kinetic model fitting parameters are determined with the same approach exploited for the homogeneous GUVs.

3. Results

Mono-RL and di-RL have been separated by the commercial rhamnolipids using a column chromatography, according to the method reported on Sect. 2.1. Prior to microscope experiments, we determined the CMC of either mono-RL and di-RL, both in water and in 0.2 M glucose solution. Measurements were performed with the surface tension technique at temperature $(23 \pm 1)^\circ \text{C}$, as described in the Sect. 2.2. Plots of the surface tension as a function of RLs concentration are shown in Fig. S3 of SI, where the best fits with piece-wise straight lines are also reported. Results indicated that the CMC for mono-RL is $0.093 \pm 0.005 \text{ mM}$ in water and $0.062 \pm 0.005 \text{ mM}$ in 0.2 M glucose solution and, for di-RL, CMC is $0.054 \pm 0.005 \text{ mM}$ in water and $0.028 \pm 0.005 \text{ mM}$ in 0.2 M glucose solution.

GUV samples were prepared by the electroformation method and dispersed in 0.2 M glucose solution for optimum visualization on the phase contrast microscope. All details are described in the Sect. 2.3. Optical microscopy experiments, in both phase contrast and fluorescence modes, were performed on GUVs formed by

ternary mixture of DOPC:SM:CHOL at molar ratio 1:1:1 in the presence of 0.1 mol % of fluorescence probe Rho-PE in the membrane, which preferentially partitions into L_d phases [24]. A first series of microscope observations was performed in the absence of RLs, for the sake of control. Fig. S4 of the SI shows a representative fluorescence snapshot for the investigated system. It is evident that all the GUVs have a spherical shape, indicating the absence of any frustration process. We also notice that GUVs show L_d - L_o phase coexistence: the brilliant white micro-scale phases are in fact due to the presence of the fluorescence probe Rho-PE inserted in the L_d phase mainly formed by DOPC. We have then carried out experiments for GUVs in the presence of three selected concentrations of either mono-RL or di-RL. As we did not know *a priori* the partition of both biosurfactants to the membrane in respect to the solution, experiments were done at concentrations near and above CMC in glucose solution as follows.

3.1. Shape analysis of GUVs images

Microscope images in phase contrast and fluorescence mode of GUVs in the presence of mono-RL and di-RL are shown in Figs. 4 and 5. In both figures, panels A, B and C refer to 0.06, 0.12 and 0.25 mM, respectively. Each panel shows representative snapshots of one GUV, carefully selected from the first of three repeated experiments (a part the unique experiment for di-RL at 0.25 mM, see Sect. 2.4) taken at different times (shown in the bottom left corner) elapsed after mixing GUVs and RLs solutions. These snapshots are aligned in the top row of each panel. The bottom row of each panel contains the same snapshots of the top row, to which the best regular or distorted circles obtained by the **ImageJ** macro (see Sec. 2.5) have been added. The complete set of snapshots analysed with the macro, from which the images shown in Figs. 4 and 5 are taken, is shown in Figs. S6-S8 and Figs. S20-S22 of the SI. All the images of the repeated experiments are reported in Figs. S10-S12, S15-S17, S24-S25 and S28-S29 of the SI. Noteworthy, whereas the incubation of mono-RL with L_o - L_d phase separated membrane immediately promoted lipid mixing, identified by a homogeneous Rh-PE distribution (Fig. 4), di-RL conducted to L_o outward budding over time (Fig. 5). Interestingly, this latter effect was also previously reported by incubating the commercial mono and di-RL mixture with the same model plasma membrane [8]. However, here we further observe that di-RL can also promote a change in L_d phase permeability to sugar molecules depending on biosurfactant concentration (Fig. 5, panels B and C). In order to separate the main roles of mono and di-RL on plasma membrane models, we now proceed the analysis by evaluating changes in surface area,

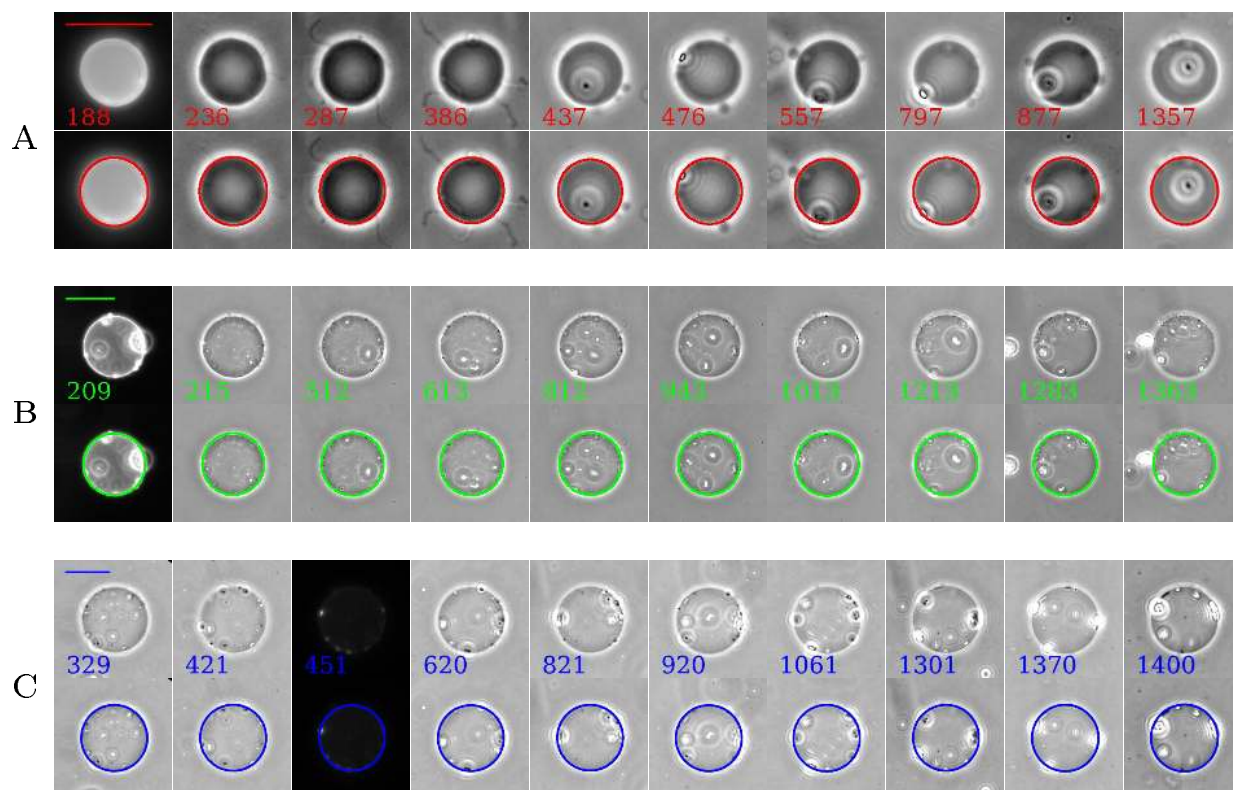


Figure 4: Representative DOPC:SM:CHOL (1:1:1) GUV fluorescence and phase contrast images dispersed in 0.06 mM, 0.12 mM and 0.25 mM mono-RL (panels A, B and C respectively). The time sequence, expressed in seconds in the bottom left corner of each image, refers to the elapsed time after mixing RLs with GUV solution, which is time 0 s. The images located above in each panel were superimposed with the best circle surrounding the GUVs and then determined with an ImageJ macro, which corresponds to the images located below. The top left bars span 20 μm .

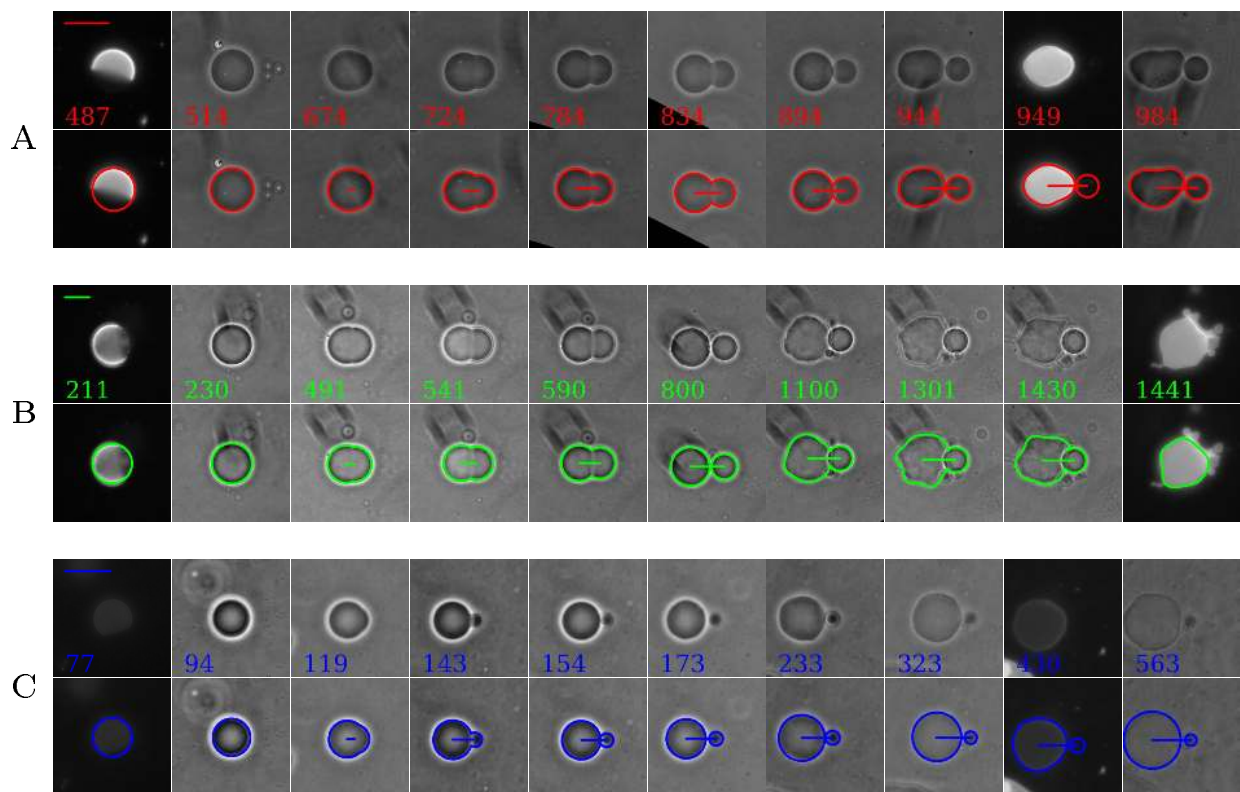


Figure 5: Representative DOPC:SM:CHOL (1:1:1) GUV fluorescence and phase contrast images dispersed in 0.06 mM, 0.12 mM and 0.25 mM di-RL (panels A, B and C respectively). See caption of Fig. 4 for other details.

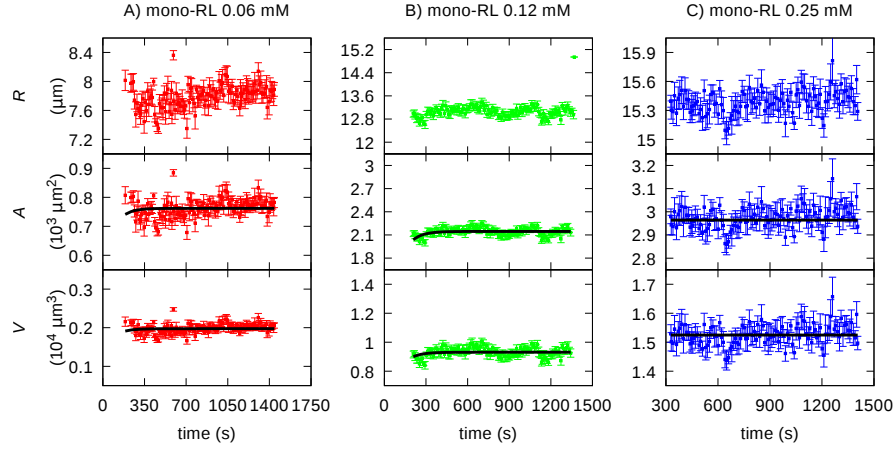


Figure 6: Time-dependence of the geometrical parameters of DOPC:SM:CHOL (1:1:1) GUVs in the presence of 0.06 mM, 0.12 mM and 0.25 mM (red, green and blue circles respectively) mono-RL (panels A, B and C). Panels A to C: the top plot corresponds to GUVs average radius, the second one to the GUVs area, the third one to the GUV volume. Error bars show the standard deviation on the parameters calculated as described in Sect. 2.5. Solid black lines are the best fit of area and volume obtained with Eq. 18 and 21, respectively. Residual plots are shown in Fig. S9 of SI.

volume and permeability as described in Sec. 2.5.

3.1.1. Shape analysis of mono-rhamnolipid GUVs

Concerning the interaction of mono-RL on DOPC:SM:CHOL GUVs, the biosurfactant at 0.06 mM (at CMC) not just favors lipid mixing, but leads to filaments formation in the first 400 s, followed by a significant protrusion over the membrane surface and the appearance of small buds (see snapshot of 437 s Fig. 4, panel A, for instance) that are kept over time. This must be due to the mono-RL insertion in the outer membrane leaflet affecting the spontaneous membrane curvature. Interestingly, the area excess released through filaments/buds/membrane protrusion practically preserves the area/volume of the original GUV, as shown by the measured values of radius R , area A and volume V (Eqs. 2, 9 and 10, respectively) displayed on Fig. 6, panel A. For 0.12 mM and 0.25 mM mono-RL concentrations, the effects on DOPC:SM:CHOL GUVs are rather similar (Fig. 4, panels B and C): the GUVs spherical shape and dimension are preserved over incubation time (Fig. 6, panels B and C), no membrane permeability increase is observed, with the appearance of small dots over the membrane surface (dark dots in phase contrast mode and fluorescent dots in fluorescence mode - Fig. 4, panels B and C). We thus speculate that such dots must represent complex aggregates composed of lipids, mono-RL and

Rh-PE fluorophore molecules of dimensions of few microns. Similar results have been obtained by the repeated experiments as shown in Figs. S13 and S18 of the SI.

3.1.2. Shape analysis of di-rhamnolipid GUVs

For two-phase-domain GUVs, observed with di-RL, we have determined the average radii of L_d and L_o phases (R_d and R_o , respectively), the distance between the centers of the two phases (r_{do}) and the related values of areas (A_α , with $\alpha = d, o$, Eq. 12) and volumes (V_α , Eq. 13). As an example, the Table S2 in SI shows all the fitting and derived parameters obtained with the ImagJ macro related to the two-phase-domain GUV seen for 0.12 mM di-RL at $t = 1100$ s (Fig. 5, panel B, 7th image from left to right). Parameters of all the images are plotted as a function of the time in Fig. 7. Similarly to results described on Ref. [8] in experiments performed with a commercial mono-RL/di-RL mixture, the L_o phase, which appears dark in fluorescence mode, is outwardly budding. The novelty here observed is that during the experiment time, the L_d phase shows shape and size fluctuation and loss of phase contrast, whereas the L_o phase remains with its initial circular shape. In the experiment performed with 0.06 mM di-RL (Fig. 5, panel A), the protrusion of L_o phase starts after 600 s in contact with di-RL, with 0.12 mM after 400 s (Fig. 7, panel B) and at 0.25 mM (Fig. 7, panel C) the protrusion occurs before 200 s, suggesting that the concentration of di-RL has a impact on L_o phase protrusion. Results obtained by repeating other two times the same experiments, shown in Figs. S26 and S30, confirm this behavior. A detailed comparison of the distance between the centers of L_d and L_o phases (r_{do}) for three repeated experiments by using 0.06 mM di-RL is outlined in Fig. S5 of SI. Analyzing each of the three time profiles $r_{do}(t)$ with a simple logistic function (written in the caption of Fig. S5) and plotting the ratios of $r_{do}(t)$ to the asymptotic behavior r_{do}^∞ , one can observe a remarkable similarity of the three repeated experiments.

Also in the presence of 0.12 and 0.25 mM di-RL the ternary DOPC:SM:CHOL 1:1:1 GUV has a significant loss of contrast, with the L_d phase becoming almost transparent by the end of the experiment (Fig. 5, panel C). The plots of area and volume for 0.06 and 0.12 mM di-RL (panels A and B on Fig. 7) show that, after the protrusion of the L_o phase, both the L_d area, A_d , and the total area, A , increase, whereas A_o (the area of the L_o phase) has a slight decrease, suggesting that the main contribution to the increase of A derives from A_d and thus revealing that the most important effect of di-RL on the plasma membrane is its insertion in the L_d phase, as previously observed for the mixture.

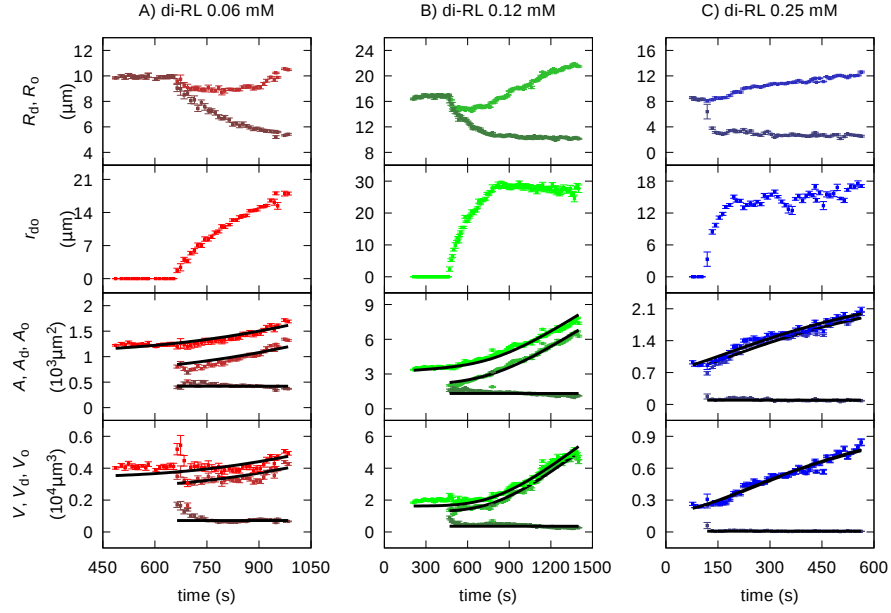


Figure 7: Time-dependence of the geometrical parameters of DOPC:SM:CHOL (1:1:1) GUVs in the presence of 0.06 mM, 0.12 mM and 0.25 mM (red, green and blue circles respectively) di-RL (panels A, B and C). Panels A to C: the top plot corresponds to the average radius of the GUV L_d phase (intermediate-shade colors) and L_o phase (dark-shade colors); the second plot reports the distance between the center of the L_d phase and the one of the L_o phase; the third plot reports the L_d phase GUV area (intermediate shade color) and the best fit obtained with Eq. 27 (with $\alpha = d$, solid black lines), the L_o phase GUV area (dark-shade color) and the best fit obtained with Eq. 27 (with $\alpha = o$, solid black lines), and the total GUV area with the best fit obtained with Eq. 27 (by the sum for $\alpha = d, o$, solid black line); the fourth plot reports the L_d phase GUV volume (intermediate shade color) and the best fit obtained with Eq. 28 (with $\alpha = d$, solid black lines), the L_o phase GUV volume (dark-shade color) and the best fit obtained with Eq. 28 (with $\alpha = o$, solid black lines), and the total GUV volume with the best fit obtained with Eq. 28 (by the sum for $\alpha = d, o$, solid black line). Error bars show the standard deviation on the parameters calculated as described in Sect. 2.5. Residual plots are shown in Fig. S23 of SI.

Panel B on Fig. 7 shows that up to 800 s the volume of GUV in the presence of 0.12 mM di-RL is constant, the area of the L_d phase slightly increases and the one of the L_o phase does not change. This result indicates that di-RL gets into the membrane only via the L_d phase, without significantly increasing its permeability to the solution. Conversely, after 800 s, the GUV volume increases, due to the increase of membrane permeability that determines an exchange between inner and outer solution, with a concomitant decrease of the optical contrast, as seen in Fig. 5, panel B. Panel C of Fig. 7 (0.25 mM di-RL) shows that both volume and area of L_d phase increase, indicating that up to the beginning of the experiment the GUV permeability increases allowing the inner/outer membrane solution exchange. The results from these optical microscope observations emphasize that the insertion of di-RL molecules is favored in the L_d phase of DOPC:SM:CHOL (1:1:1 molar ratio), promoting initially L_o outward budding, followed by an increase in surface area and permeability of L_d phase with increasing di-RL concentration. This must be due to its molecular structure with large polar head area in comparison to the hydrophobic chain in a cone-shaped geometry [4]. This must favor pore formation (see ahead in the text) via micelle-like solubilization process. On the other hand, mono-RL promotes lipid mixing instead. Such a fact must be related to its molecular structure that favors planar structures as unilamellar vesicles [4], thus preserving the original GUVs spontaneous curvature.

3.2. Kinetics of rhamnolipids-GUVs interaction

3.2.1. Mono-rhamnolipid-GUVs interaction

A detailed analysis of the time-behavior of areas and volumes of DOPC:SM:CHOL 1:1:1 GUVs in the presence of mono-RL has been performed by applying the kinetic model introduced in Sec. 2.6 (Eqs. 18 and 21). Fitting curves are shown as black solid lines in Fig. 6 and for the other two repeated experiments in Figs. S13 and S30 of SI. The kinetic model fitting parameters of the three independent analyses are displayed in Tables S3, S4 and S5 of SI. Since a remarkable similarity of the parameters for the three replicas has been found (excluding N and V_0 that can only be specific of the analyzed GUV), for each parameter the mean value and the standard deviation over the replicas have been calculated. Results are shown in Table 1. It should be stressed that, although no increase in membrane permeability has been here experimentally observed by mono-RL interaction, the theoretical modeling opens the possibility to include pore formation as possible biosurfactant/lipid bilayer mechanism (Sec. 2.6). Doing so, the data analysis demonstrated that the insertion

		mono-RL 0.06 mM	mono-RL 0.12 mM	mono-RL 0.25 mM
		A	B	C
N	(10^9)	2.43 ± 0.06	1.11 ± 0.03	2.66 ± 0.03
V_0	$(10^4 \mu\text{m}^3)$	0.135 ± 0.006	0.389 ± 0.008	0.42 ± 0.06
$\langle \lambda_1 \rangle$	(μm)	2.90 ± 0.03	2.87 ± 0.03	5.1 ± 0.1
$\langle \lambda_2 \rangle$	(μm)	17 ± 2	28.1 ± 0.8	29.7 ± 0.3
$\langle r_p \rangle$	(\AA)	2.78 ± 0.07	3.8 ± 0.1	4.48 ± 0.07
$\langle m \rangle$		1.30 ± 0.01	1.06 ± 0.01	1.14 ± 0.03
$\langle n \rangle$		9.8 ± 0.1	7.1 ± 0.2	1.25 ± 0.04
$\langle pk_{1+} \rangle$	$(\langle k_{1+} \rangle \text{ in } \text{s}^{-1}\text{M}^{-m})$	-2.57 ± 0.03	-2.20 ± 0.03	-1.79 ± 0.06
$\langle pk_{1-} \rangle$	$(\langle k_{1-} \rangle \text{ in } \text{s}^{-1})$	4.6 ± 0.6	4.9 ± 0.6	5.1 ± 0.6
$\langle pk_{2+} \rangle$	$(\langle k_{2+} \rangle \text{ in } \text{s}^{-1}\text{M}^{1-n})$	-94 ± 3	73 ± 1	23 ± 1
$\langle pk_{2-} \rangle$	$(\langle k_{2-} \rangle \text{ in } \text{s}^{-1})$	225 ± 4	148 ± 3	27.8 ± 0.5

Table 1: Parameters obtained by the simultaneous best fit with the kinetic model of the DOPC:SM:CHOL 1:1:1 GUV areas and volumes in the presence of mono-RL shown as solid black lines in Fig. 6. The parameters reported in angular brackets have been calculated by averaging the values obtained from the fit of three independent experiments (see Tables S3, S4 and S5 of SI).

of mono-RL in the membrane is the dominant process with no pore formation (see ahead in the text, Fig. 8). Furthermore, a perusal of the fitting parameters from Table 1 reveals some interesting features. The kinetic order $\langle m \rangle$ is ≈ 1.2 , slightly decreasing with mono-RL concentration. Similarly, the constant $\langle \lambda_1 \rangle$, which quantifies the correlation between area and volume time rate (Eq. 19), maintains a steady value of $\approx 3 \mu\text{m}$ up to 0.12 mM, which slightly increase to $\approx 5 \mu\text{m}$ at 0.25 mM. On the other hand, the direct kinetic constant of the RL-insertion process, $\langle pk_{1+} \rangle$ slightly changes from ≈ -2.4 (with k_{1+} expressed in $\text{s}^{-1}\text{M}^{-1.3}$) to ≈ -1.8 . The corresponding reverse kinetic constants, $\langle pk_{1-} \rangle$ (with $\langle k_{1-} \rangle$ expressed in s^{-1}), show positive values, with an average of ≈ 5 , indicating a much slower rate.

A marked discontinuity on going from 0.06 mM mono-RL to 0.12 mM is observed considering the parameters describing the pore formation process. However, it should be noticed that in all cases a very small pore radius $r_p \approx 3 - 4 \text{\AA}$ has been found, which practically suggests the absence of pores able to increase membrane permeability to sugar molecules.

In detail, from Table 1, we observe that the constant $\langle \lambda_2 \rangle$ describing the time dependency of $V_2(t)$ (Eq. 20) changes from $(3.2 \pm 0.4) \mu\text{m}$ at 0.06 mM to $\approx 30 \mu\text{m}$ at 0.12 and 0.25 mM. The kinetic order, $\langle n \rangle$, changes from ≈ 10 to ≈ 1 , the direct kinetic constant, $\langle pk_{2+} \rangle$, from ≈ -94 (with $\langle k_{2+} \rangle$ expressed in $\text{s}^{-1}\text{M}^{-10}$) to ≈ 23 ($\langle k_{2+} \rangle$ is in $\text{s}^{-1}\text{M}^{-1}$ units), and the reverse kinetic constant, $\langle pk_{2-} \rangle$ (with $\langle k_{2-} \rangle$ expressed in

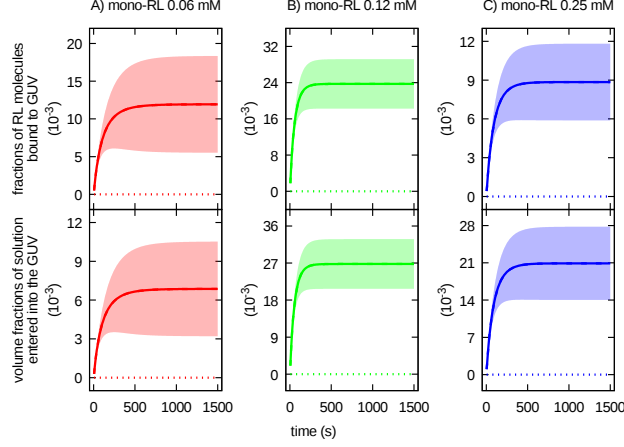


Figure 8: Fractions of mono-RL molecules bound to GUVs (top panels) and volume fractions of solution entering into GUVs (bottom panels) as a function of time after the contact between GUV and mono-RL solutions. The color type is related to the mono-RL concentration: 0.06 mM, red; 0.12 mM, green; 0.25 mM, blue. The line type is related to the different RL:GUV interaction mechanism: dashed, fraction due to RL-insertion, $f_1(t)$ (top panel) or $V_1(t)/V(t)$ (bottom panel); dotted, fraction due to pore formation, $f_2(t)$ (top panel) or $V_2(t)/V(t)$ (bottom panel); solid, sum of the effects of both mechanisms, $f(t)$ (top panel) or $(V_1(t) + V_2(t))/V(t)$ (bottom panel). The shaded band represents the standard deviation obtained by considering the uncertainties of the kinetic model parameters, averaged over three experimental replicas, reported in Table 1.

s^{-1}), from the high and positive value ≈ 225 to ≈ 28 . The overall effect of these parameters can be better understood by evaluating the time dependency of the fraction $f(t)$ of mono-RLs bound to the GUVs, which, according to the two foreseen mechanisms of RL-insertion and pore formation, is the sum of $f_1(t)$ and $f_2(t)$, respectively. Plots of $f(t)$, $f_1(t)$ and $f_2(t)$, obtained by the fitting parameters shown in Table 1, are reported in Fig. 8 as solid, dashed and dotted line, respectively. The standard deviation of these time trends, shown as a shaded band in Fig. 8, has been obtained by sampling the values of the fitting parameters shown between angular brackets in Table 1 from a Gaussian having the parameter's standard deviation. A number of 100 samplings has been used. We notice that, in general, these fractions are quite small in the order of 10^{-3} , suggesting a preferential mono-RL partition to the glucose solution. Furthermore, we see that at any mono-RL concentration the fraction of molecules forming the pores is negligible and the mono-RL molecules insert likely in the outer leaflet. We have also calculated the volume fractions of the solution that has entered into the GUV through the two mechanisms, $V_1(t)/V(t)$ and $V_2(t)/V(t)$, respectively. Results are reported in the bottom panels of Fig. 8 as dashed and dotted lines, respectively, and their sum as a solid line. The shaded bands represent the standard deviations obtained by using the same method described above. We observe that the

		di-RL 0.06 mM A	di-RL 0.12 mM B	di-RL 0.25 mM C
N_d	(10^9)	1.90 ± 0.04	5.67 ± 0.08	2.0 ± 0.1
$V_{d,0}$	$(10^4 \mu\text{m}^3)$	0.273 ± 0.007	1.27 ± 0.01	0.183 ± 0.005
$\langle \lambda_{d,1} \rangle$	(μm)	0.109 ± 0.003	0.087 ± 0.003	0.087 ± 0.004^a
$\langle \lambda_{d,2} \rangle$	(μm)	3.2 ± 0.4	8.85 ± 0.09	6.5 ± 0.1^a
$\langle r_{d,p} \rangle$	(\AA)	500 ± 5	494 ± 5	500 ± 5^a
$\langle m_d \rangle$		1.07 ± 0.01	1.02 ± 0.01	1.00 ± 0.01^a
$\langle n_d \rangle$		3.44 ± 0.03	4.12 ± 0.04	1.27 ± 0.01^a
$\langle pk_{d1+} \rangle$	$(\langle k_{d1+} \rangle \text{ in } s^{-1} M^{-m_d})$	-0.244 ± 0.003	0.059 ± 0.001	-0.2 ± 0.1^a
$\langle pk_{d1-} \rangle$	$(\langle k_{d1-} \rangle \text{ in } s^{-1})$	10.7 ± 0.8	11.0 ± 0.8	6 ± 1^a
$\langle pk_{d2+} \rangle$	$(\langle k_{d2+} \rangle \text{ in } s^{-1} M^{1-n_d})$	-31.6 ± 0.3	-41.8 ± 0.4	2.12 ± 0.06^a
$\langle pk_{d2-} \rangle$	$(\langle k_{d2-} \rangle \text{ in } s^{-1})$	38.2 ± 0.4	39.4 ± 0.4	6.12 ± 0.06^a
N_o	(10^9)	2.27 ± 0.02	7.36 ± 0.07	0.517 ± 0.005
$V_{o,0}$	$(10^4 \mu\text{m}^3)$	0.059 ± 0.003	0.359 ± 0.004	0.0061 ± 0.0007
$\langle \lambda_{o,1} \rangle$	(μm)	10.4 ± 0.1	8.5 ± 0.1	8.3 ± 0.2^a
$\langle \lambda_{o,2} \rangle$	(μm)	29.9 ± 0.3	30.0 ± 0.3	29.5 ± 0.4^a
$\langle r_{o,p} \rangle$	(\AA)	500 ± 5	479 ± 7	480 ± 10^a
$\langle m_o \rangle$		1.08 ± 0.02	1.60 ± 0.03	1.1 ± 0.1^a
$\langle n_o \rangle$		7.26 ± 0.07	7.3 ± 0.1	7.3 ± 0.2^a
$\langle pk_{o1+} \rangle$	$(\langle k_{o1+} \rangle \text{ in } s^{-1} M^{-m_o})$	0.189 ± 0.004	0.301 ± 0.007	0.19 ± 0.03^a
$\langle pk_{o1-} \rangle$	$(\langle k_{o1-} \rangle \text{ in } s^{-1})$	5.0 ± 0.6	4.0 ± 0.6	3.1 ± 0.8^a
$\langle pk_{o2+} \rangle$	$(\langle k_{o2+} \rangle \text{ in } s^{-1} M^{1-n_o})$	69.2 ± 0.8	124 ± 1	83 ± 5^a
$\langle pk_{o2-} \rangle$	$(\langle k_{o2-} \rangle \text{ in } s^{-1})$	62.5 ± 0.9	93 ± 2	64 ± 4^a

Table 2: Parameters obtained by the simultaneous best fit of the DOPC:SM:CHOL 1:1:1 GUV areas and volumes in the presence of di-RL shown as solid black lines in Fig. 7. The parameters reported in angular brackets have been calculated by averaging the values obtained from the fit of three independent experiments (see Tables S6, S7 and S8 of SI). ^a Values obtained by experiment n. 1.

overall volume fraction is low, in the order of 10^{-3} , increases with the mono-RL concentration, and its only due to the RL-insertion process, suggesting that mono-RL has a negligible effect in modifying DOPC:SM:CHOL 1:1:1 membrane permeability to sugar molecules.

3.2.2. Di-rhamnolipid-GUVs interaction

Let us now consider the interpretation with the kinetic model, in the two-phase-domain version (see. Sect. 2.6.2), of GUV volume and area in the presence of di-RL. Best fitting curves are shown as solid black lines in Fig. 7, for the first experiment of each concentration, and in Figs. S26 and S30 of the SI for the two replicas. The fitting parameters of each experiment are reported in Tables S6, S7 and S8 of the SI.

Notice that in each of the three tables the same values for the unique 0.25 mM experiment are reported in

the last column, for the sake of a better comparison with the parameters of the other two concentrations shown in the two previous columns. Due to the high similarity of the kinetic model parameters for the three replicas of each experimental conditions, the replicas' averages and standard deviations have been calculated. Results are reported in Table 2. We first notice that the kinetic order $\langle m_d \rangle$ of the RL-insertion process occurring in the L_d phase is ≈ 1 , at any di-RL concentration. On the other hand, the related direct kinetic constant, $\langle pk_{d1+} \rangle$ (with $\langle k_{1+} \rangle$ expressed in $s^{-1}M^{-1}$) shows small values comprised between ≈ -0.2 and ≈ 0 . The constants of the reverse kinetic process, $\langle pk_{d1-} \rangle$ (with $\langle k_{d1-} \rangle$ expressed in s^{-1}), are much higher and change from ≈ 11 to ≈ 6 , confirming a variation of the di-RL-GUV interaction with the di-RL concentration as observed. Beside, also the constant $\langle \lambda_{d,1} \rangle$ changes with the amount of di-RL, although remaining in the order of $0.1 \mu m$. Parameters regarding the pore formation mechanism of di-RL into the L_d phase confirm the marked dependency on di-RL concentration. Indeed, the kinetic orders, $\langle n_d \rangle$, are found to be quite different, varying from ≈ 1 to ≈ 4 . Hence it is difficult to make a comparison among direct kinetic constants, pk_{d2+} , since the unit of $\langle k_{d2+} \rangle$ ($s^{-1}M^{1-n_d}$) changes with $\langle n_d \rangle$. Conversely, the reverse constant, $\langle pk_{d2-} \rangle$ (with $\langle k_{d2-} \rangle$ expressed in s^{-1}), can be compared: they change from ≈ 40 at 0.06 and 0.12 mM to only 6.12 ± 0.06 at 0.25 mM, confirming a strong concentration dependency of the pore formation mechanism. Likewise, the constant $\langle \lambda_{d,2} \rangle$ changes with di-RL concentration in the range $\approx 3 - 9 \mu m$. To note, the average pore radius is found to be $\approx 500 \text{ \AA}$, for all the investigated conditions.

Regarding the interaction of di-RL with the DOPC:SM:CHOL 1:1:1 L_o domain, the kinetic model parameters are shown in the second block of Table 2. The kinetic order of the di-RL-insertion process, $\langle m_o \rangle$, is comprised in the small range 1.0–1.6 and smooth variations are also found for the related direct kinetic constant $\langle pk_{o1+} \rangle$, despite the unit of $\langle k_{o1+} \rangle$ ($s^{-1}M^{-m_o}$) depends on $\langle m_o \rangle$. The reverse kinetic constants $\langle pk_{o1-} \rangle$ is between ≈ 3 and ≈ 5 and the large values of $\langle \lambda_{o,1} \rangle \approx 9 \mu m$ are quite independent of di-RL concentration. Looking to the parameters describing the pore formation process occurring at the L_o phase, we notice a constant value of the kinetic order $\langle n_o \rangle \approx 7.3$, a very large and steady value of the proportionality constant $\langle \lambda_{o,2} \rangle \approx 30 \mu m$, as well as an almost constant value of the pore radius $\langle r_{o,p} \rangle \approx 500 \text{ \AA}$. On the contrary, the direct kinetic constants $\langle pk_{o2+} \rangle$ change in the range ≈ 70 to ≈ 120 , whereas the reverse kinetic constants $\langle pk_{o2-} \rangle$ change from ≈ 60 to ≈ 90 .

By using the set of kinetic fitting parameters describing the interaction of di-RL with DOPC:SM:CHOL 1:1:1 GUVs and averaged over the repeated experiments (Table 2), we have subsequently calculated the fractions of di-RL molecules involved in the two L_d and L_o phases and in the two foreseen processes (RL-insertion and pore formation), as well as the volume fraction of the solution that has entered into the GUV via the two mechanisms. Results are shown in Fig. 9 together with their standard deviations depicted with shaded bands. We notice that, in general, the fraction of di-RL bound to the GUV are in the order of $10^{-4} - 10^{-3}$, in line with the values detected for mono-RL or for the commercial mixture of mono and di-RL [8]. More in detail, we see that at 0.06 mM di-RL (Fig. 9, top panel A) most of the di-RL molecules are bound via the first mechanism (diRL-insertion) occurring over the L_d phase (intermediate-shade-dotted line), with a fraction that at the longest times seems to reach a steady value of $\approx 1.5 \cdot 10^{-3}$. We also notice that, after ≈ 600 s from the beginning of the experiment, the fraction due to pore formation in the L_d phase starts to grow, without reaching a steady value, at least within the duration of the measurements. The contribution to the total fraction (brilliant-solid line) due to di-RL molecules interacting with the L_o phase is only caused by diRL-insertion mechanism (dark-shade-dashed line superimposed with the dark-shade-solid lines) accounting for $\approx 2 \cdot 10^{-4}$, being the one due to pore formation totally negligible (dark-shade-dotted line close to 0). Looking at the volume fractions of the solution entering into the GUV (Fig. 9, bottom panel A), we see that, as expected, the L_d phase is mostly involved (intermediate-shade lines very close to the brilliant-solid lines). After ≈ 500 s from the beginning of the experiment, the contribution due to pore formation (intermediate-shade-dotted line) in L_d is ≈ 0.2 , similar to the one due to diRL-insertion and the possible concomitant increase of membrane permeability (intermediate-shade-dashed line), and then becomes much higher, ≈ 0.6 . Hence, despite the fraction of di-RL forming pores in L_d ($f_{d,2}(t)$) is lower than the one just embedded in L_d ($f_{d,1}(t)$), mostly of the solution entering in the GUV passes through the pores and not from the possible increase of the membrane permeability due to the RL-insertion mechanism. Results at the highest concentrations of di-RL are easier to understand, since no contribution due to L_o phase (dark-shade lines all ≈ 0) has been observed. At 0.12 mM di-RL the fraction of molecules bound to the GUV via the diRL-insertion mechanism (Fig. 9, top panel B, intermediate-shade-dashed line superimposed with the intermediate-shade-solid line) continuously grows and reaches a maximum of $\approx 10^{-3}$, very similar to the corresponding value at 0.06 mM di-RL, after ≈ 500 s from the beginning of the

experiment. Also the volume of the solution entering into the GUV due to this mechanism (Fig. 9, bottom panel B, intermediate-shade-dashed line superimposed with the brilliant-shade-dashed line) reaches a maximum of ≈ 0.2 , as for the 0.06 mM di-RL case. Moreover, from 500 s onward, the fraction of di-RL forming pores at the L_d phase (Fig. 9, top panel B, intermediate-shade-dotted line superimposed with the brilliant-shade-dotted line) grows up apparently without reaching a steady value and the volume fraction of the solution entering through these pores (Fig. 9, bottom panel B, intermediate-shade-dotted line superimposed with the brilliant-shade-dotted line) also grows to more than ≈ 0.6 . At 0.25 mM di-RL the whole process occurs at shorter times: the maximum volume fraction solution entering into the GUV by the diRL-insertion mechanism (Fig. 9, bottom panel C, intermediate-shade-dashed line superimposed with the brilliant-shade-dashed line) is again ≈ 0.2 and it is reached after ≈ 200 s from the beginning of the experiment. Therefore, the kinetic model analysis clearly demonstrated that di-RL has a preferential binding site on L_d phase in respect to L_o phase, followed by pore formation above a di-RL concentration threshold.

4. Conclusion

It is well known that rhamnolipids, with a significant tensioactive and emulsifying properties, have different applications as environmental bio-remediation, bio-medicines, food and cosmetics, which have motivated the growing research activity to characterize their biochemical and structural properties [3].

Here we studied the interactions between model membranes represented by GUVs and mono-RL and di-RL molecules, showing how it is possible, by assuming a kinetic model, to derive relevant physical parameters from optical microscopy images. Furthermore, membranes composed of DOPC:SM:CHOL at 1:1:1 molar ratio were used as plasma model membranes which display L_o - L_d lipid domains (mimicking lipid rafts). Interestingly, we determined that although a low fraction of RLs indeed interacts with the lipid bilayer (fraction on the order of 10^{-3}), these impose a significant impact on membrane features. Regarding the mono-RL effect on lipid domains, we show that RLs must insert mainly in the outer membrane leaflet revealed by the observation of excess of membrane area (protusion, buds and filaments formation) coupled to the phases coexistence disappearance. We may attribute this latter effect to the molecular structure of mono-RL that favors planar structures as unilamellar vesicles [4]. In this way, its insertion in either L_d or L_o phase does not cause any lipid packing

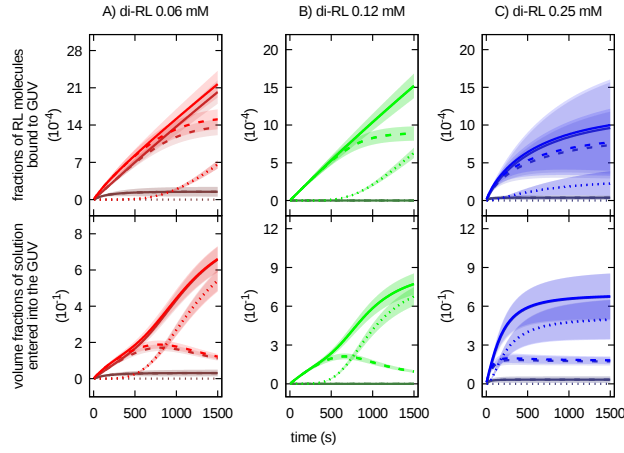


Figure 9: Fractions of di-RL bound to GUVs (top panels) and volume fractions of solution entering into GUVs (bottom panels) as a function of time after the contact between GUV and di-RL solutions. The color type is related to the di-RL concentration: 0.06 mM, red; 0.12 mM, green; 0.25 mM, blue. Top panels: intermediate-shade-dashed lines: $f_{d,1}(t)$; intermediate-shade-dotted lines: $f_{d,2}(t)$; intermediate-shade-solid lines: $f_d(t) = f_{d,1}(t) + f_{d,2}(t)$; dark-shade-dashed lines: $f_{o,1}(t)$; dark-shade-dotted lines: $f_{o,2}(t)$; dark-shade-solid lines: $f_o(t) = f_{o,1}(t) + f_{o,2}(t)$; brilliant-dashed lines: $f_1(t) = f_{d,1}(t) + f_{o,1}(t)$; brilliant-dotted lines: $f_2(t) = f_{d,2}(t) + f_{o,2}(t)$; brilliant-solid lines: $f(t) = f_1(t) + f_2(t)$. Bottom panels: intermediate-shade-dashed lines: $V_{d,1}(t)/V(t)$; intermediate-shade-dotted lines: $V_{d,2}(t)/V(t)$; intermediate-shade-solid lines: $(V_{d,1}(t) + V_{d,2}(t))/V(t)$; dark-shade-dashed lines: $V_{o,1}(t)/V(t)$; dark-shade-dotted lines: $V_{o,2}(t)/V(t)$; dark-shade-solid lines: $(V_{o,1}(t) + V_{o,2}(t))/V(t)$; brilliant-dashed lines: $(V_{d,1}(t) + V_{o,1}(t))/V(t)$; brilliant-dotted lines: $(V_{d,2}(t) + V_{o,2}(t))/V(t)$; brilliant-solid lines: $(V_{d,1}(t) + V_{o,1}(t) + V_{d,2}(t) + V_{o,2}(t))/V(t)$. The shaded band represents the standard deviation obtained by considering the uncertainties of the kinetic model parameters, averaged over three experimental replicas for 0.06 and 0.12 mM di-RL and only calculated by the fit procedure (see the end of Sec. 2.6.2) for the single experiment at 0.25 mM di-RL (Table 2).

frustration and may permit lipid mixing.

On the other hand, in the experiments performed with di-RL, differently from the mono-RL experiments, the ternary GUVs kept the L_d - L_o phase coexistence but the presence of di-RLs conducts to L_o outward budding with incubation time. The di-RL-GUV interaction occurs basically in the L_d domain, since, after the L_o protusion due to di-RL insertion, L_d domain loses shape and contrast due to pore formation process, while L_o remains practically intact. Indeed, di-RL-GUV interaction increases as the di-RL concentration grows, both for di-RL-insertion and pore formation processes. Such fact must be related to the particular cone-shaped molecular structure of di-RL [4] that imposes high curvature surfaces.

To note, the more marked interaction effect of di-RL with DOPC:SM:CHOL 1:1:1 GUV system, when compared with mono-RL, is in agreement with the results we have previously obtained by investigating the commercial RL mixture richer in di-RL (2:1 di-RL:mono-RL molar ratio) interacting with the same type of GUV [8]. Indeed, the outwardly budding of the L_o phase is seen in the presence of both the di-RL alone and the commercial RL mixture. Moreover, also for the commercial mixture case, we found a difference between the fractions of RL molecules bound to the L_d and L_o GUV domains.

Finally, the importance of this work is twofold. From one hand, a new methodology has been introduced, aimed to derive from observations with the phase-contrast microscope a kinetic model of interaction between surfactants and model membranes constituted by lipid domains. On the other hand, the information obtained for the two main components of RL, mono-RL and di-RL, are relevant for the potential biotechnological applications of this fascinating class of biosurfactant. Noteworthy, both biosurfactants may cause damage on plasma membranes: mono-RL promotes lipid mixing thus affecting cell signaling and di-RL inducing L_o outward budding and permeability increase (pore formation) that may also conduct to cell homeostasis loss and eventually cell death.

Declaration of Competing Interest

The authors declare that they have no known competing financial interests or personal relationships that could have appeared to influence the work reported in this paper.

CRediT authorship contribution statement

Alessandra Marega Motta: Investigation, Writing - Original Draft. **Maressa Donato:** Investigation. **Giovanna Mobbili:** Investigation. **Paolo Mariani:** Validation. **Rosangela Itri:** Conceptualization, Writing- Original draft, Supervision, Funding acquisition. **Francesco Spinozzi:** Conceptualization, Writing- Original draft, Formal analysis, Methodology, Software, Writing - Review & Editing, Supervision.

Acknowledgments

RI is recipient from Conselho Nacional de Pesquisa (CNPq, Brazil) for research fellowship.

Appendix A. Supplementary data

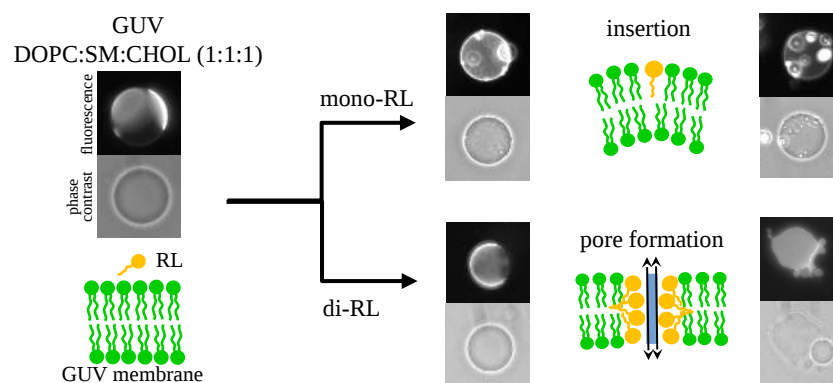
Supplementary data to this article can be found online at ... (file **SI.pdf**).

- [1] F. L. Martínez, N. B. Moraga, N. Romano-Armada, M. F. Yañez-Yazlle, V. B. Rajal, V. Irazusta, Step-wise Strategies for the Bioremediation of Contaminated Soils: From the Microbial Isolation to the Final Application, Springer International Publishing, Cham, 2018, pp. 1–28.
- [2] E. Rosenberg, E. Z. Ron, High- and low-molecular-mass microbial surfactants, *Applied Microbiology and Biotechnology* 52 (1999) 154–162.
- [3] H. Abbasi, K. A. Noghabi, M. M. Hamed, H. S. Zehri, A. A. Moosavi-Movahedi, M. Amanlou, J. A. Teruel, A. Ortiz, Physicochemical characterization of a monorhamnolipid secreted by *Pseudomonas aeruginosa* MA01 in aqueous media. An experimental and molecular dynamics study, *Colloids and surfaces. B, Biointerfaces* 101 (2013) 256–265.
- [4] M. L. Chen, J. Penfold, R. K. Thomas, T. J. P. Smyth, A. Perfumo, R. Marchant, I. M. Banat, P. Stevenson, A. Parry, I. Tucker, I. Grillo, Solution self-assembly and adsorption at the air-water interface of the monorhamnolipid and dirhamnolipids and their mixtures, *Langmuir* 26 (2010) 18281–18292.
- [5] A. P. Karlapudi, T. Venkateswarulu, J. Tammineedi, L. Kanumuri, B. K. Ravuru, V. ramu Dirisala, V. P. Kodali, Role of biosurfactants in bioremediation of oil pollution-a review, *Petroleum* 4 (2018) 241–249.
- [6] M. Benincasa, A. Abalos, I. Oliveira, A. Manresa, Chemical structure, surface properties and biological activities of the biosurfactant produced by *Pseudomonas aeruginosa* LBI from soapstock, *Antonie van Leeuwenhoek* 85 (2004) 1–8.
- [7] M. Sánchez, J. A. Teruel, M. J. Espuny, A. Marqués, F. J. Aranda, A. Manresa, A. Ortiz, Modulation of the physical properties of dielaidoylphosphatidylethanolamine membranes by a dirhamnolipid biosurfactant produced by *pseudomonas aeruginosa*, *Chemistry and physics of lipids* 142 (2006) 118–127.
- [8] B. Come, M. Donato, L. F. Potenza, P. Mariani, R. Itri, F. Spinozzi, The intriguing role of rhamnolipids on plasma membrane remodelling: From lipid rafts to membrane budding, *Journal of Colloid and Interface Science* 582 (2021) 669–677.
- [9] Faucon, J.F., Mitov, M. D., Méléard, P., Bivas, I., Bothorel, P., Bending elasticity and thermal fluctuations of lipid membranes. theoretical and experimental requirements, *J. Phys. France* 50 (1989) 2389–2414.

- [10] P. Méléard, T. Pott, H. Bouvrais, J. H. Ipsen, Advantages of statistical analysis of giant vesicle flickering for bending elasticity measurements, *The European Physical Journal E* 34 (2011) 116.
- [11] T. Bhatia, P. Husen, J. Brewer, L. A. Bagatolli, P. L. Hansen, J. H. Ipsen, O. G. Mouritsen, Preparing giant unilamellar vesicles (guvs) of complex lipid mixtures on demand: Mixing small unilamellar vesicles of compositionally heterogeneous mixtures, *Biochimica et Biophysica Acta (BBA) - Biomembranes* 1848 (2015) 3175–3180.
- [12] M. Chabanon, P. Rangamani, Solubilization kinetics determines the pulsatory dynamics of lipid vesicles exposed to surfactant, *Biochimica et Biophysica Acta (BBA) - Biomembranes* 1860 (2018) 2032–2041.
- [13] A. Helenius, K. Simons, Solubilization of membranes by detergents, *Biochimica et Biophysica Acta (BBA) - Reviews on Biomembranes* 415 (1975) 29–79.
- [14] T. H. Haines, Water transport across biological membranes, *FEBS Letters* 346 (1994) 115–122.
- [15] D. W. Deamer, J. Bramhall, Permeability of lipid bilayers to water and ionic solutes, *Chemistry and Physics of Lipids* 40 (2) (1986) 167–188.
- [16] D. R. Perinelli, D. Vllasaliu, G. Bonacucina, B. Come, S. Pucciarelli, M. Ricciutelli, M. Cespi, R. Itri, F. Spinozzi, G. F. Palmieri, L. Casettari, Rhamnolipids as epithelial permeability enhancers for macromolecular therapeutics, *European Journal of Pharmaceutics and Biopharmaceutics* 119 (2017) 419 – 425.
- [17] F. J. Aranda, M. J. Espuny, A. Marqués, J. A. Teruel, A. Manresa, A. Ortiz, Thermodynamics of the interaction of a dirhamnolipid biosurfactant secreted by *pseudomonas aeruginosa* with phospholipid membranes, *Langmuir* 23 (2007) 2700–2705.
- [18] A. M. Abdel-Mawgoud, F. Lépine, E. Déziel, Rhamnolipids: diversity of structures, microbial origins and roles, *Applied Microbiology and Biotechnology* (2010) 1323–1336.
- [19] E. Boisselier, E. Demers, L. Cantin, C. Salesse, How to gather useful and valuable information from protein binding measurements using langmuir lipid monolayers, *Advances in Colloid and Interface Science* 243 (2017) 60–76.

- [20] A. G. Ayuyan, F. S. Cohen, Lipid peroxides promote large rafts: Effects of excitation of probes in fluorescence microscopy and electrochemical reactions during vesicle formation, *Biophysical Journal* 91 (2006) 2172–2183.
- [21] N. F. Morales-Pennington, J. Wu, E. R. Farkas, S. L. Goh, T. M. Konyakhina, J. Y. Zheng, W. W. Webb, G. W. Feigenson, Guv preparation and imaging: Minimizing artifacts, *Biochimica et Biophysica Acta (BBA) - Biomembranes* 1798 (2010) 1324–1332.
- [22] C. A. Schneider, W. S. Rasband, K. W. Eliceiri, Nih image to imagej: 25 years of image analysis, *Nature Methods* 9 (2012) 671–675.
- [23] E. I. Organick, *A FORTRAN IV Primer*, Addison-Wesley, 1966, p. 42.
- [24] S. L. Veatch, S. L. Keller, Seeing spots: Complex phase behavior in simple membranes, *Biochimica et Biophysica Acta (BBA) - Molecular Cell Research* 1746 (2005) 172 – 185.

Graphical abstract



Supplementary Information

Unveiling the mono-rhamnolipid and di-rhamnolipid mechanisms of action upon plasma membrane models

Alessandra Marega Motta^a, Maressa Donato^b, Giovanna Mobbili^a, Paolo Mariani^a, Rosangela Itri^b
and Francesco Spinozzi^a

^a Department of Life and Environmental Sciences, Polytechnic University of Marche, Italy

^b Institute of Physics, University of São Paulo, Brazil

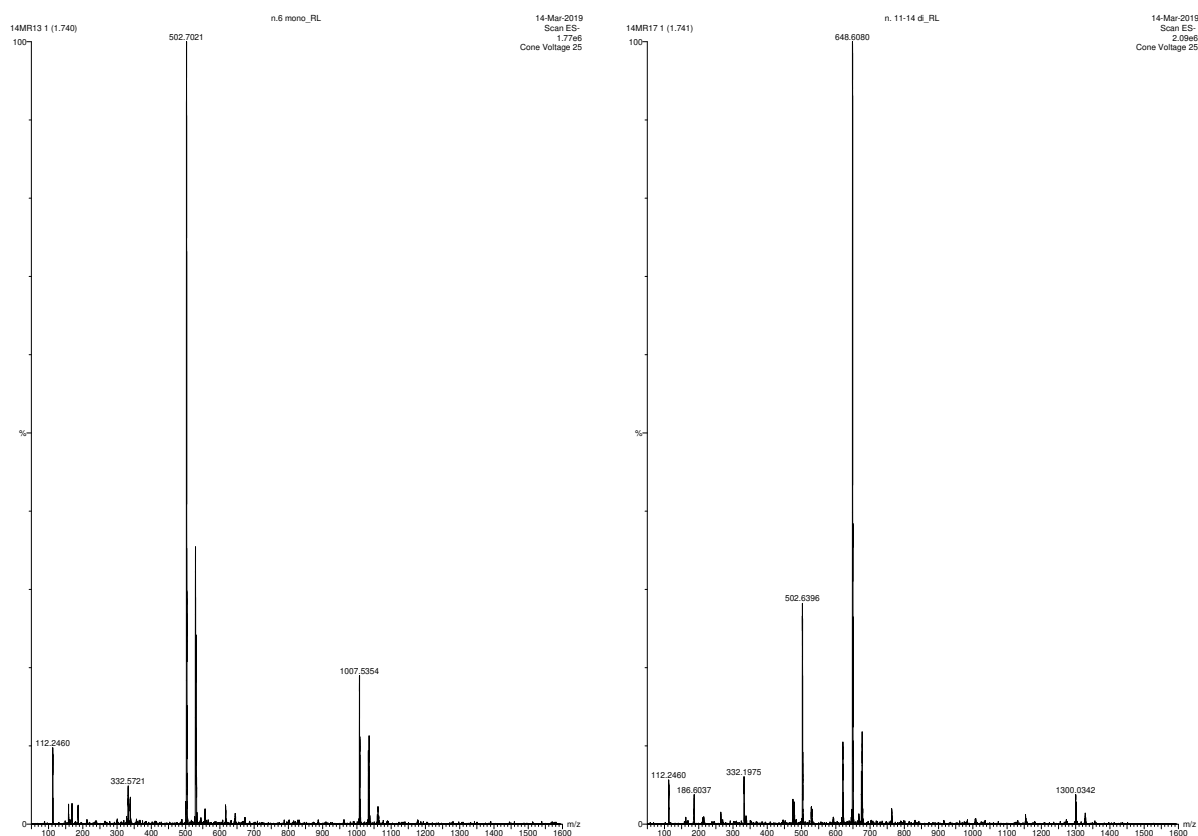


Figure S1: Electrospray mass spectroscopy profiles of mono-RL (left) and di-RL (right).

S1 Test of a asymmetric GUV contour determination

Test cases of the approach described in the “Materials and Methods” to determine the contour of an asymmetric GUV are shown in Fig. S2. The red line represents the true contour of the GUV seen by the microscope. Green points $\{x_i, y_i\}$ are the ones selected by the users, that could be affected by a 5% error with respect to the position in the red contour. The blue contour is the one obtained as best fit of the green point by the method, and within this blue contour, the magenta points $\{x_{\text{fit},i}, y_{\text{fit},i}\}$ are the best approximations of the green ones. Regarding the red contour, the parameters $x_c, y_c, R, \{a_k, b_k\}$ have been randomly chosen, with $N \leq 10$ and $-1000 \leq x_c \leq 1000$, $-1000 \leq y_c \leq 1000$, $1 \leq R \leq 300$, $-0.3 \leq a_k \leq 0.3$ and $-0.3 \leq b_k \leq 0.3$. The unit length is assumed to be μm .

Results of Fig. S2 are promising: in all cases, blue and red contours are very similar.

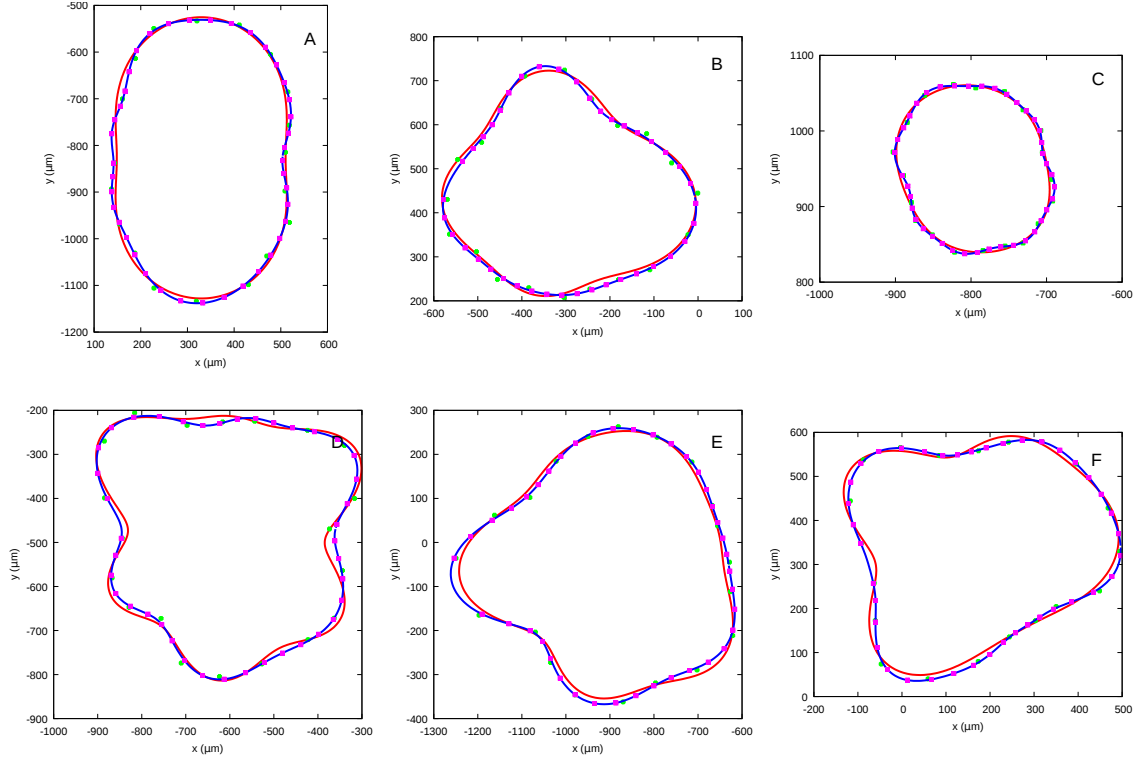


Figure S2: Six selected examples of the determination of the contour of a GUV seen by optical microscope. See Sect. S1 for details. The fitting parameters of panels A-F (with a_i and b_i multiplied by the factor 10^2) are hereafter listed. A) $x_c = 322 \pm 5 \mu\text{m}$, $y_c = -822 \pm 7 \mu\text{m}$, $R = 241.6 \pm 0.4 \mu\text{m}$, $a_1 = -2 \pm 2$, $b_1 = 4 \pm 3$, $a_2 = 1.1 \pm 0.2$, $b_2 = -24.3 \pm 0.3$, $a_3 = 1.2 \pm 0.6$, $b_3 = -2.3 \pm 0.6$, $a_4 = 0.8 \pm 0.4$, $b_4 = 1.5 \pm 0.3$, $a_5 = -0.8 \pm 0.3$, $b_5 = -1.8 \pm 0.3$, $a_6 = -0.1 \pm 0.4$, $b_6 = -0.9 \pm 0.2$, $a_7 = 1.6 \pm 0.3$, $b_7 = 0.3 \pm 0.2$, $a_8 = -0.4 \pm 0.2$, $b_8 = -1.1 \pm 0.4$. B) $x_c = -317 \pm 6 \mu\text{m}$, $y_c = 439 \pm 3 \mu\text{m}$, $R = 249.1 \pm 0.6 \mu\text{m}$, $a_1 = 2 \pm 1$, $b_1 = 6 \pm 2$, $a_2 = -3.5 \pm 0.3$, $b_2 = 6.3 \pm 0.3$, $a_3 = -8.3 \pm 0.4$, $b_3 = 5.3 \pm 0.3$, $a_4 = 1.8 \pm 0.3$, $b_4 = 8.2 \pm 0.5$, $a_5 = 0.8 \pm 0.5$, $b_5 = -2.0 \pm 0.5$, $a_6 = -1.2 \pm 0.3$, $b_6 = -0.8 \pm 0.3$, $a_7 = -1.2 \pm 0.3$, $b_7 = 0.4 \pm 0.3$, $a_8 = 0.6 \pm 0.2$, $b_8 = 0.3 \pm 0.3$. C) $x_c = -797 \pm 2 \mu\text{m}$, $y_c = 945 \pm 3 \mu\text{m}$, $R = 106.5 \pm 0.3 \mu\text{m}$, $a_1 = 5 \pm 3$, $b_1 = 2 \pm 2$, $a_2 = -6.1 \pm 0.5$, $b_2 = -5.7 \pm 0.5$, $a_3 = -0.4 \pm 0.6$, $b_3 = 1.3 \pm 0.6$, $a_4 = -2.3 \pm 0.4$, $b_4 = -1.6 \pm 0.5$, $a_5 = -0.1 \pm 0.5$, $b_5 = -0.9 \pm 0.5$, $a_6 = -1.1 \pm 0.5$, $b_6 = 0.5 \pm 0.6$, $a_7 = 0.8 \pm 0.6$, $b_7 = 0.5 \pm 0.6$, $a_8 = -2.4 \pm 0.5$, $b_8 = 0.2 \pm 0.4$, $a_9 = -0.7 \pm 0.5$, $b_9 = 0.2 \pm 0.6$. D) $x_c = -609 \pm 6 \mu\text{m}$, $y_c = -467 \pm 7 \mu\text{m}$, $R = 290.1 \pm 0.5 \mu\text{m}$, $a_1 = -5 \pm 2$, $b_1 = 2 \pm 2$, $a_2 = -4.2 \pm 0.3$, $b_2 = -1.9 \pm 0.3$, $a_3 = 10.2 \pm 0.4$, $b_3 = -0.4 \pm 0.4$, $a_4 = 1.0 \pm 0.6$, $b_4 = -7.0 \pm 0.2$, $a_5 = -1.9 \pm 0.7$, $b_5 = 0.4 \pm 0.4$, $a_6 = 3.4 \pm 0.3$, $b_6 = -6.5 \pm 0.3$, $a_7 = 0.6 \pm 0.7$, $b_7 = 0.3 \pm 0.4$, $a_8 = -1.5 \pm 0.2$, $b_8 = -0.7 \pm 0.2$. E) $x_c = -885 \pm 7 \mu\text{m}$, $y_c = -49 \pm 6 \mu\text{m}$, $R = 290.0 \pm 0.4 \mu\text{m}$, $a_1 = -2 \pm 2$, $b_1 = -5 \pm 2$, $a_2 = -1.4 \pm 0.3$, $b_2 = -0.7 \pm 0.4$, $a_3 = -3.1 \pm 0.4$, $b_3 = -8.9 \pm 0.4$, $a_4 = -2.0 \pm 0.7$, $b_4 = 7.6 \pm 0.3$, $a_5 = -2.3 \pm 0.4$, $b_5 = -6.6 \pm 0.4$, $a_6 = 2.4 \pm 0.4$, $b_6 = 1.1 \pm 0.4$, $a_7 = -0.2 \pm 0.2$, $b_7 = -0.1 \pm 0.3$, $a_8 = 0.8 \pm 0.2$, $b_8 = 0.4 \pm 0.2$. F) $x_c = 157 \pm 7 \mu\text{m}$, $y_c = 343 \pm 10 \mu\text{m}$, $R = 274.6 \pm 0.6 \mu\text{m}$, $a_1 = -2 \pm 4$, $b_1 = 3 \pm 3$, $a_2 = 6.7 \pm 0.8$, $b_2 = 8.0 \pm 0.7$, $a_3 = 10.0 \pm 0.7$, $b_3 = 11.1 \pm 0.5$, $a_4 = -7.9 \pm 0.9$, $b_4 = -2.5 \pm 0.6$, $a_5 = 0.1 \pm 0.5$, $b_5 = 2.5 \pm 0.8$, $a_6 = -0.6 \pm 0.4$, $b_6 = 1.9 \pm 0.2$, $a_7 = -1.4 \pm 0.3$, $b_7 = -0.2 \pm 0.2$, $a_8 = 0.3 \pm 0.2$, $b_8 = 0.4 \pm 0.2$, $a_9 = -0.4 \pm 0.2$, $b_9 = 0.2 \pm 0.3$, $a_{10} = -0.4 \pm 0.3$, $b_{10} = -0.7 \pm 0.2$.

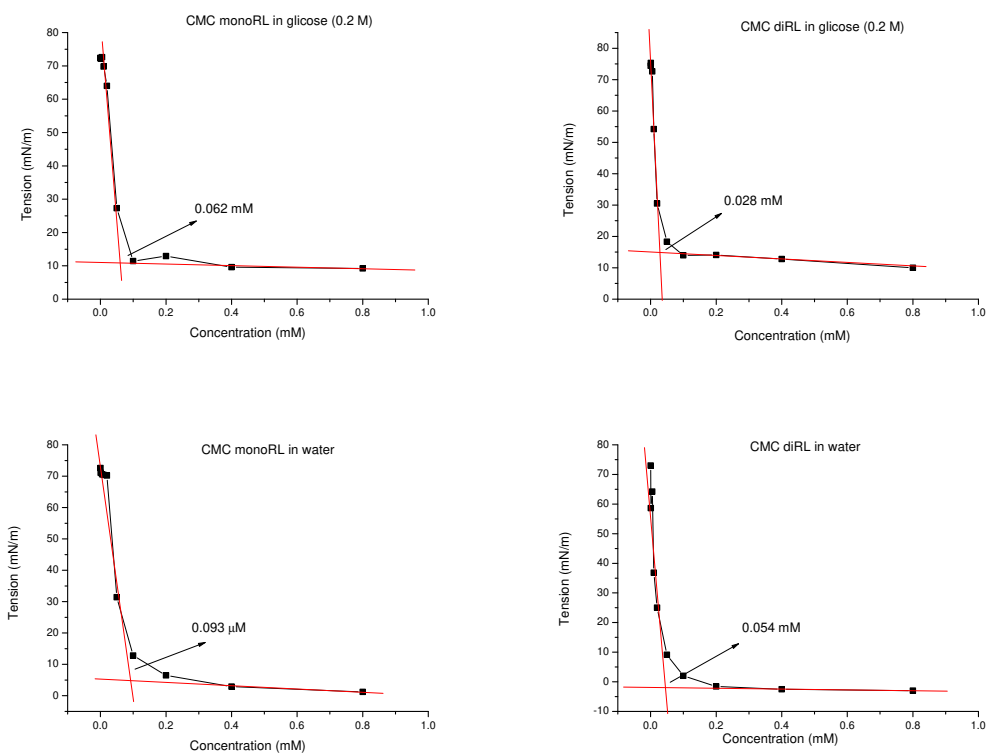


Figure S3: Surface tension measurements and related CMC determination for mono-RL and di-RL in 0.2 M glucose and in water.

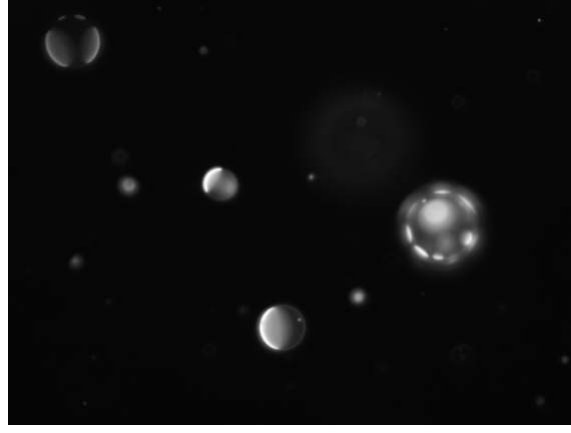


Figure S4: Representative optical microscope images, in fluorescence mode, of GUVs formed DOPC:SM:CHOL 1:1:1 in the presence of 0.2 M glucose and 0.1 mol % Rho-PE. For all systems the overall w/v lipid concentration is 0.00286 g/L.

S2 Determination of the molecular parameters of the GUV:RL systems

We consider a GUV formed by mixing n lipid molecules (\mathbf{L}_i , with $i = 1, n$), according to mixing mole ratios x_i . In our case \mathbf{L}_i can be POPC, DOPC, SM or CHOL. Hence the average molecule constituting the GUV will be represented by the formula $(1/\sum_i x_i)\mathbf{L}_{1,x_1}\mathbf{L}_{2,x_2}\dots\mathbf{L}_{n,x_n}$, hereafter shortly indicated by \mathbf{E} . If the GUV shows $L_d - L_o$ phase separation, we can distinguish, among the n molecules, n_d molecules that form the L_d phase and n_o molecules that form the L_o phase. In particular, the average molecule constituting the L_d phase of the GUV will be represented by the formula $(1/\sum_{i \in L_d} x_i)\mathbf{L}_{i_1,x_{i_1}}\mathbf{L}_{i_2,x_{i_2}}\dots\mathbf{L}_{i_{n_d},x_{i_{n_d}}}$, being i_1, i_2, \dots the indexes of the n_d molecules that form the L_d phase. We indicate this formula by \mathbf{E}_d . Likewise, the average molecule constituting the L_o phase of the GUV has the formula $(1/\sum_{i \in L_o} x_i)\mathbf{L}_{i_1,x_{i_1}}\mathbf{L}_{i_2,x_{i_2}}\dots\mathbf{L}_{i_{n_o},x_{i_{n_o}}}$, being i_1, i_2, \dots the indexes of the n_o molecules that form the L_o phase. We call in short this formula \mathbf{E}_o . Let M_i and a_i the molecular weight and the area per polar head of the i -molecule. On this basis, we can calculate the average molecular weight and the average area per polar head by referring to the effective molecule \mathbf{E} forming the whole GUV (a and M , respectively) as well as to both the molecules \mathbf{E}_d forming the GUV L_d phase (a_d and M_d , respectively) and the molecules \mathbf{E}_o forming

C_{RL} mM	C μM	C_{d} μM	C_{o} μM	a \AA^2	a_{d} \AA^2	a_{o} \AA^2	ζ	ζ_{d}	ζ_{o}
0.06	4.56	1.52	3.04	45.3	64.0	36.0	13.2	39.5	19.7
0.12	4.56	1.52	3.04	45.3	64.0	36.0	26.3	78.9	39.5
0.25	4.56	1.52	3.04	45.3	64.0	36.0	54.8	164.4	82.2

Table S1: Molar concentrations, areas per polar heads and nominal RL-to-lipid ratios of all the investigated GUV-RL systems. Letters refer to figures and tables of the main text. C_{RL} is the molar concentration of either mono-RL or di-RL. C is the molar concentration of \mathbf{E} , the average lipid molecule forming the GUV. C_{d} and C_{o} are the molar concentrations of \mathbf{E}_{d} and \mathbf{E}_{o} , the average lipids molecules that, in the case of phase-separation, form the disordered and the ordered phase of the GUV, respectively. a , a_{d} and a_{o} are the areas per polar head of \mathbf{E} , \mathbf{E}_{d} and \mathbf{E}_{o} , respectively. ζ , ζ_{d} and ζ_{o} are the RL-to- \mathbf{E} , RL-to- \mathbf{E}_{d} and RL-to- \mathbf{E}_{o} nominal molar ratios, respectively.

the GUV L_{o} phase (a_{o} and M_{o} , respectively),

$$\begin{aligned}
M &= \frac{\sum_i M_i x_i}{\sum_i x_i} & a &= \frac{\sum_i a_i x_i}{\sum_i x_i} \\
M_{\text{d}} &= \frac{\sum_{i \in L_{\text{d}}} M_i x_i}{\sum_{i \in L_{\text{d}}} x_i} & a_{\text{d}} &= \frac{\sum_{i \in L_{\text{d}}} a_i x_i}{\sum_{i \in L_{\text{d}}} x_i} \\
M_{\text{o}} &= \frac{\sum_{i \in L_{\text{o}}} M_i x_i}{\sum_{i \in L_{\text{o}}} x_i} & a_{\text{o}} &= \frac{\sum_{i \in L_{\text{o}}} a_i x_i}{\sum_{i \in L_{\text{o}}} x_i}
\end{aligned} \tag{S1}$$

The molar concentration of the lipid mixture with formula \mathbf{E} forming the whole GUV is $C = c/M$, where c is the total w/v lipid concentration. Hence the molar concentrations of the lipids with formulas \mathbf{E}_{d} and \mathbf{E}_{o} that form the L_{d} and the L_{o} phases, respectively, are

$$C_{\text{d}} = C \frac{\sum_{i \in L_{\text{d}}} x_i}{\sum_i x_i} \quad C_{\text{o}} = C \frac{\sum_{i \in L_{\text{o}}} x_i}{\sum_i x_i} \tag{S2}$$

with the straightforward condition $C = C_{\text{d}} + C_{\text{o}}$. If C_{RL} is the molar concentration of RL (mono-RL or di-RL, depending on the sample), we can also calculate the nominal ratio ζ between the RL molecules in the sample and the lipid molecules \mathbf{E} forming the GUV as well as the nominal ratios of the RL molecules in the sample referred to the lipid molecules \mathbf{E}_{d} and \mathbf{E}_{o} , respectively,

$$\zeta = \frac{C_{\text{RL}}}{C} \quad \zeta_{\text{d}} = \frac{C_{\text{RL}}}{C_{\text{d}}} \quad \zeta_{\text{o}} = \frac{C_{\text{RL}}}{C_{\text{o}}} \tag{S3}$$

Notice that the condition $\zeta^{-1} = \zeta_{\text{d}}^{-1} + \zeta_{\text{o}}^{-1}$ holds. In Table S1 molar concentrations, areas per polar heads and nominal RL-to-lipid ratios of all the investigated GUV-RL systems are listed.

		L_d	L_o
$x_{c,\alpha}$	(μm)	102.7 ± 0.4	125.1 ± 0.1
$y_{c,\alpha}$	(μm)	92.3 ± 0.5	106.8 ± 0.2
R_α	(μm)	19.24 ± 0.06	10.27 ± 0.06
$a_{1,\alpha}$	(10^2)	1.43 ± 0.02	—
$b_{1,\alpha}$	(10^2)	-2.324 ± 0.003	—
$a_{2,\alpha}$	(10^2)	-1.06 ± 0.02	—
$b_{2,\alpha}$	(10^2)	-1.20 ± 0.01	—
$a_{3,\alpha}$	(10^2)	0.610 ± 0.008	—
$b_{3,\alpha}$	(10^2)	-3.20 ± 0.02	—
$a_{4,\alpha}$	(10^2)	2.56 ± 0.02	—
$b_{4,\alpha}$	(10^2)	2.50 ± 0.05	—
$a_{5,\alpha}$	(10^2)	0.005 ± 0.002	—
$b_{5,\alpha}$	(10^2)	-0.0309 ± 0.0006	—
$a_{6,\alpha}$	(10^2)	1.74 ± 0.03	—
$b_{6,\alpha}$	(10^2)	1.146 ± 0.009	—
r_{do}	(μm)	26.7 ± 0.4	
A_α	($10^3 \mu\text{m}^2$)	4.64 ± 0.03	1.20 ± 0.01
V_α	($10^4 \mu\text{m}^3$)	3.17 ± 0.03	0.319 ± 0.004

Table S2: Shape parameters of the two-phase-domain GUV seen for 0.12 mM di-RL at $t = 1100$ s (Fig. 5, panel B, 7th image from left to right). The first block of parameters have been obtained by minimizing the merit function H (Eq. 5) (with $N_F = 10$): they are the coordinates of the L_d and L_o centers ($\alpha = d, o$), the average radius and the sine and cosine expansion coefficients (Eq. 1). The second block includes parameters derived from the ones of the first block: they are the distance between the centers of the two phases and the related areas (Eq. 12) and volumes (Eq. 13). The standard deviations of all these parameters have been estimated as described in Sect. 2.5.

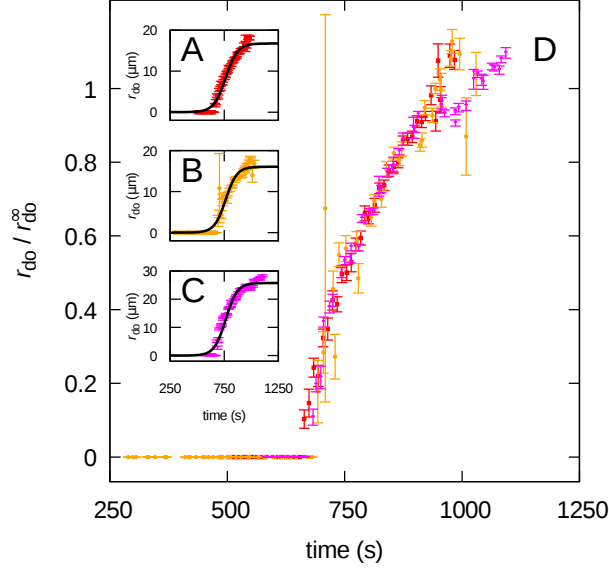


Figure S5: Time-evolution of the distance between the centers of L_d and L_o phases for GUVs in the presence of 0.06 mM di-RL. Panels A to C: results obtained with three repeated experiments as shown in Figs. 7, S26 and S30. The solid black line is the best fit obtained with the logistic function $r_{do}(t) = r_{do}^\infty [1 - \exp(t/\Delta t_{r_{do}})] / [2 - \exp(t/\Delta t_{r_{do}}) - \exp(t_{0,r_{do}}/\Delta t_{r_{do}})]$ (see Eq. 5 of Ref.¹), where r_{do}^∞ is the value at the plateau (when the time t tends to infinity), $t_{0,r_{do}}$ is time in the middle of the transition and $\Delta t_{r_{do}}$ is the time width at the transition. Fitting parameter of data in panel A: $r_{do}^\infty = (16.8 \pm 0.4) \mu\text{m}$; $t_{0,r_{do}} = (762 \pm 5) \text{ s}$; $\Delta t_{r_{do}} = (55 \pm 4) \text{ s}$. Fitting parameter of data in panel B: $r_{do}^\infty = (16.0 \pm 0.5) \mu\text{m}$; $t_{0,r_{do}} = (760 \pm 7) \text{ s}$; $\Delta t_{r_{do}} = (51 \pm 5) \text{ s}$. Fitting parameter of data in panel C: $r_{do}^\infty = (25.7 \pm 0.5) \mu\text{m}$; $t_{0,r_{do}} = (763 \pm 5) \text{ s}$; $\Delta t_{r_{do}} = (53 \pm 4) \text{ s}$. Panel D: data of panels A-C divided by the corresponding r_{do}^∞ .

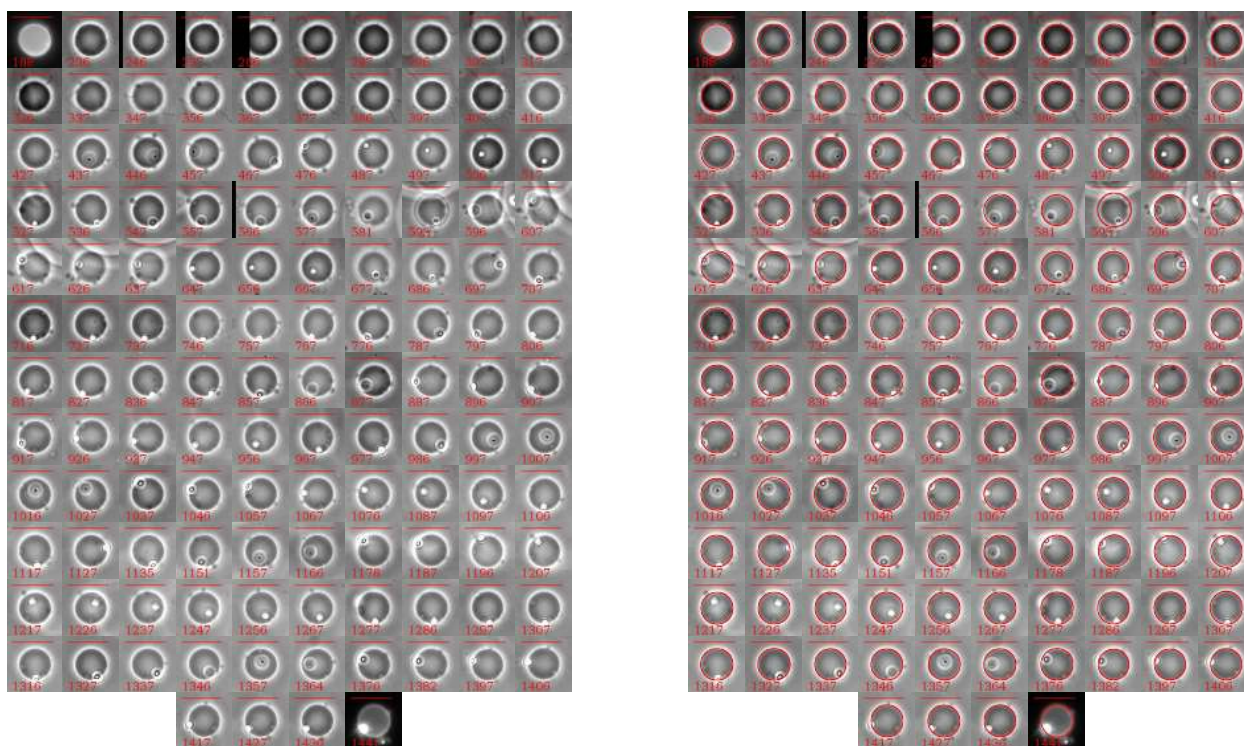


Figure S6: Microscope images (left) and best fit contours (right) of a selected DOPC:SM:CHOL 1:1:1 GUV (experiment n. 1) in the presence of 0.06 mM mono-RL.

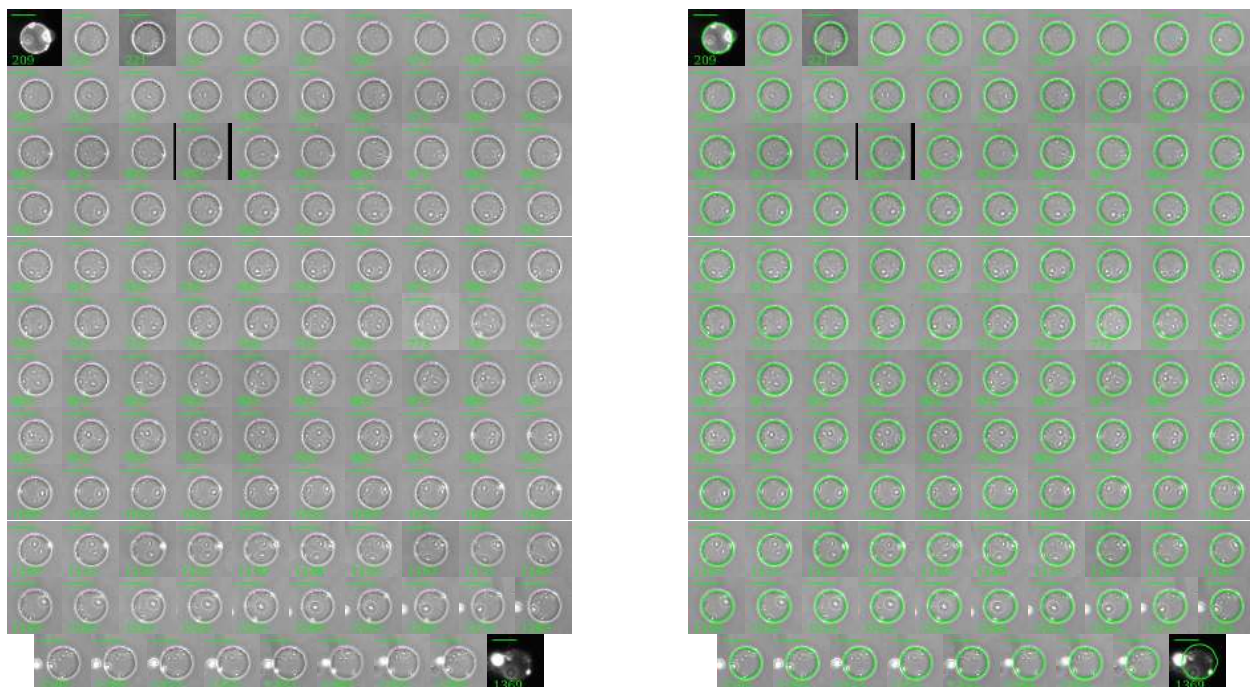


Figure S7: Microscope images (left) and best fit contours (right) of a selected DOPC:SM:CHOL 1:1:1 GUV (experiment n. 1) in the presence of 0.12 mM mono-RL.

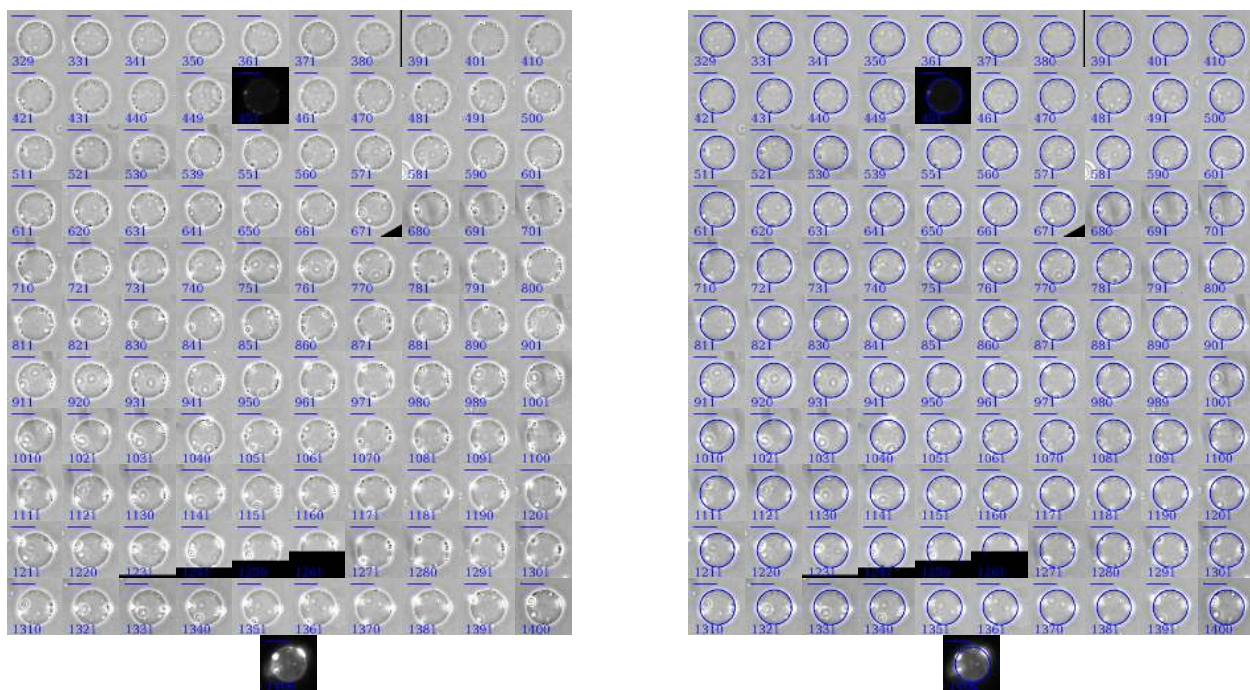


Figure S8: Microscope images (left) and best fit contours (right) of a selected DOPC:SM:CHOL 1:1:1 GUV (experiment n. 1) in the presence of 0.25 mM mono-RL.

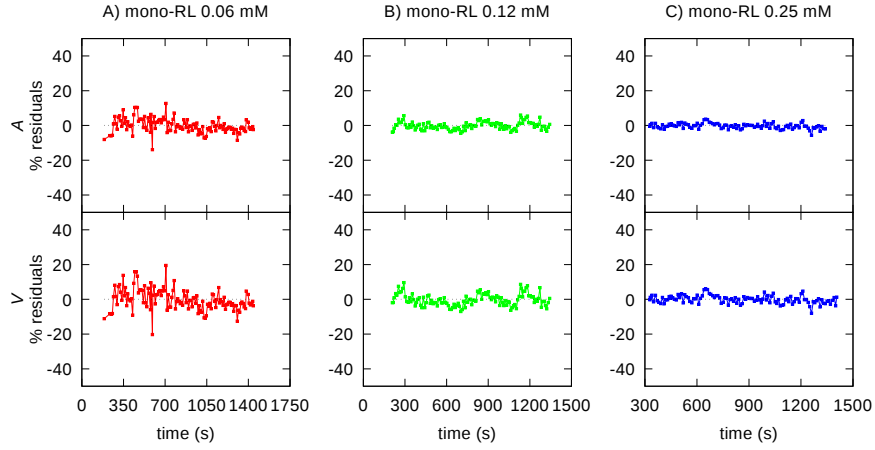


Figure S9: Residuals plots of fitting curves shown in Fig. 6.

		mono-RL 0.06 mM	mono-RL 0.12 mM	mono-RL 0.25 mM
		A	B	C
N	(10^9)	2.43 ± 0.06	1.11 ± 0.03	2.66 ± 0.03
V_0	$(10^4 \mu\text{m}^3)$	0.135 ± 0.006	0.389 ± 0.008	0.42 ± 0.06
λ_1	(μm)	2.96 ± 0.04	2.86 ± 0.05	4.7 ± 0.2
λ_2	(μm)	17 ± 3	28 ± 1	29.9 ± 0.6
r_p	(\AA)	2.8 ± 0.1	3.8 ± 0.2	4.5 ± 0.1
m		1.33 ± 0.02	1.14 ± 0.01	1.00 ± 0.07
n		9.9 ± 0.2	6.9 ± 0.5	1.26 ± 0.08
pk_{1+}	$(k_{1+} \text{ in } \text{s}^{-1}\text{M}^{-m})$	-2.21 ± 0.05	-2.50 ± 0.02	-1.9 ± 0.1
pk_{1-}	$(k_{1-} \text{ in } \text{s}^{-1})$	4.43 ± 0.04	5.67 ± 0.06	3.8 ± 0.1
pk_{2+}	$(k_{2+} \text{ in } \text{s}^{-1}\text{M}^{1-n})$	-99 ± 7	77 ± 3	21 ± 2
pk_{2-}	$(k_{2-} \text{ in } \text{s}^{-1})$	232 ± 7	158 ± 5	25 ± 1

Table S3: Parameters obtained by the simultaneous best fit of areas and volumes of the DOPC:SM:CHOL 1:1:1 GUVs (experiment n. 1, Figs. S6, S7 and S17) in the presence of mono-RL shown as solid black lines in Fig. 6.

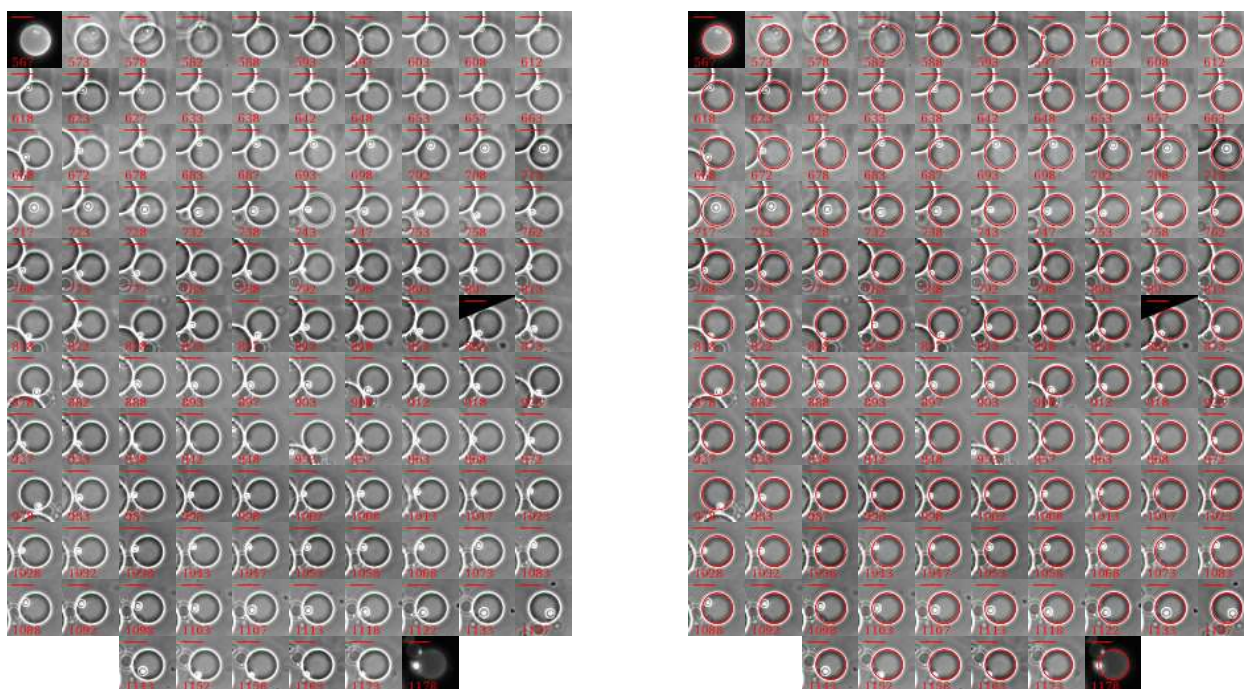


Figure S10: Microscope images (left) and best fit contours (right) of a selected DOPC:SM:CHOL 1:1:1 GUV (experiment n. 2) in the presence of 0.06 mM mono-RL.

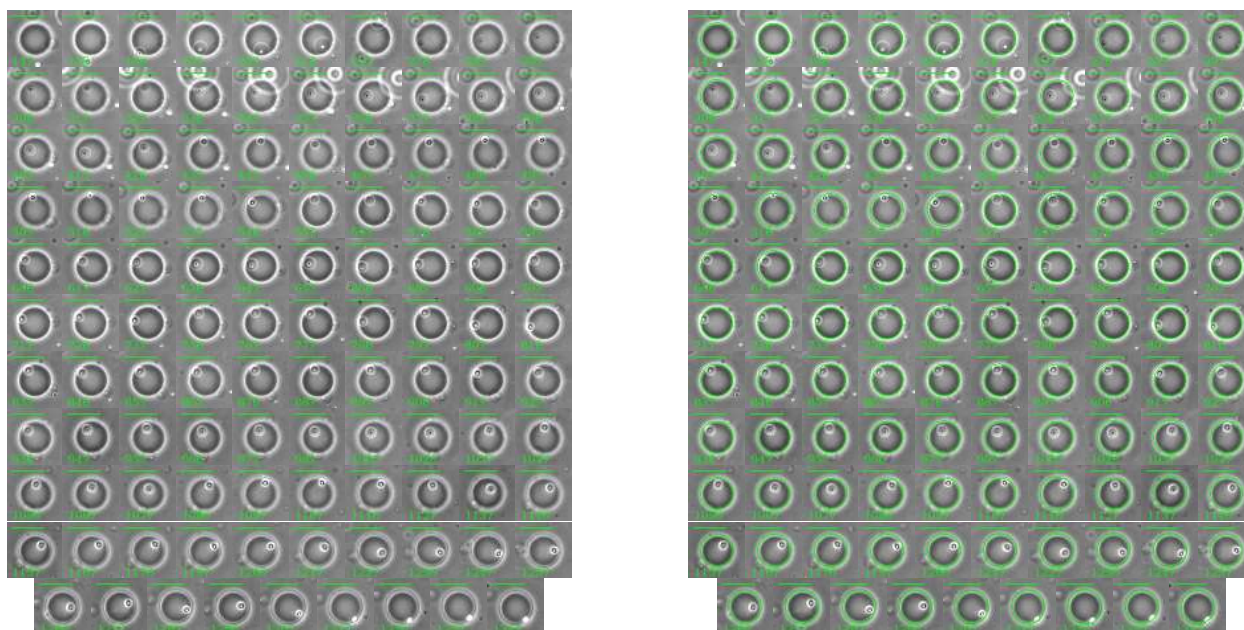


Figure S11: Microscope images (left) and best fit contours (right) of a selected DOPC:SM:CHOL 1:1:1 GUV (experiment n. 2) in the presence of 0.12 mM mono-RL.

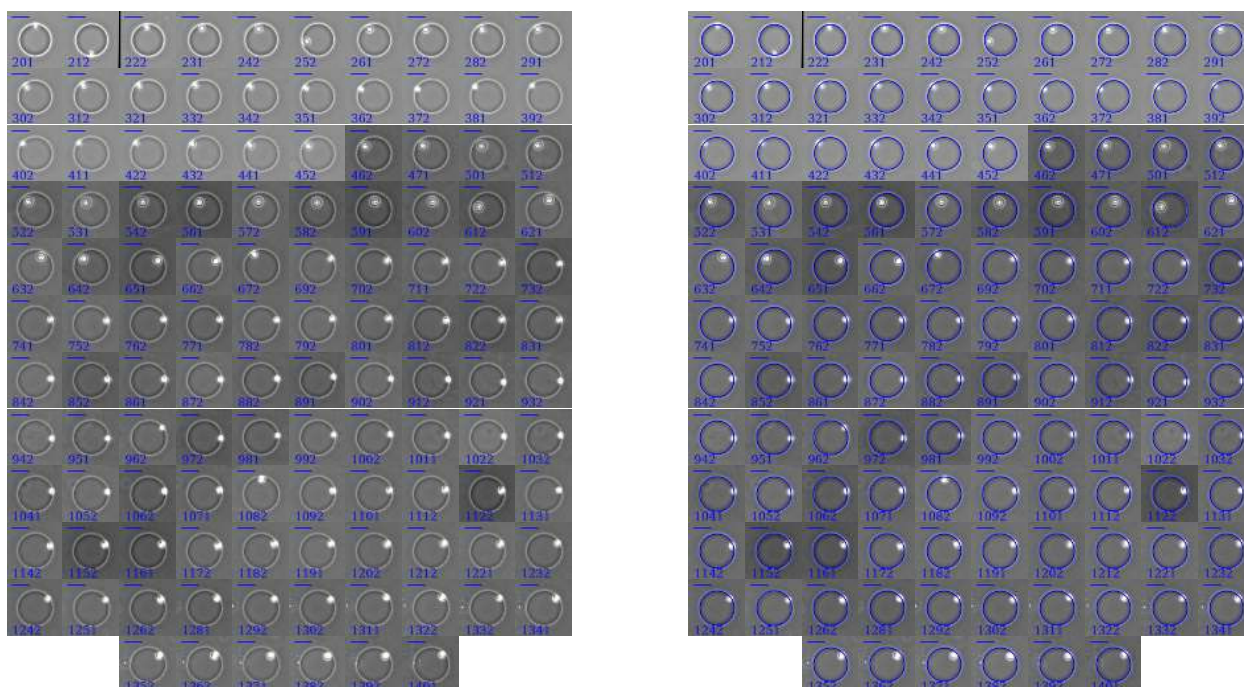


Figure S12: Microscope images (left) and best fit contours (right) of a selected DOPC:SM:CHOL 1:1:1 GUV (experiment n. 2) in the presence of 0.25 mM mono-RL.

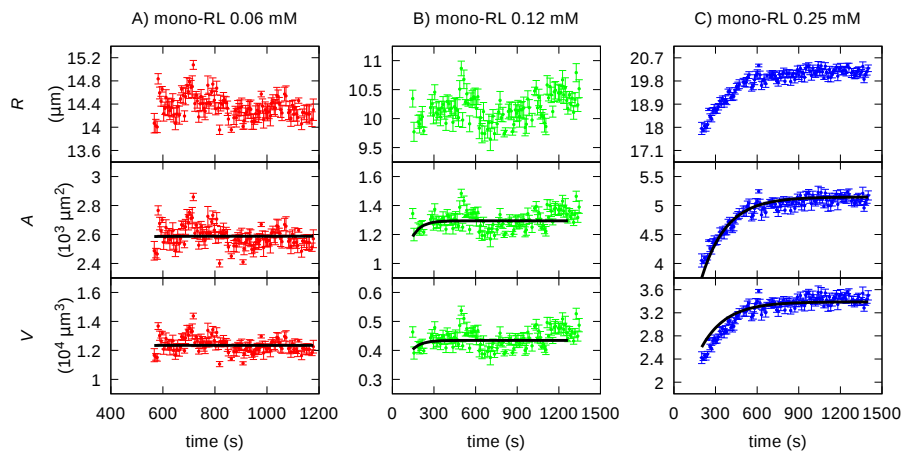


Figure S13: Time-dependence of the geometrical parameters of the DOPC:SM:CHOL (1:1:1) GUVs (experiment n. 2, Figs. S10, S11 and S17) in the presence of 0.06 mM, 0.12 mM and 0.25 mM (red, green and blue circles respectively) mono-RL (panel A, B and C). Panels A to C: the top plot corresponds to GUVs average radius, the second one to the GUV area, the third one to the GUV volume. Solid black lines are the best fit of area and volume obtained with Eq. 18 and 21, respectively. Residual plots are shown in Fig. S14.

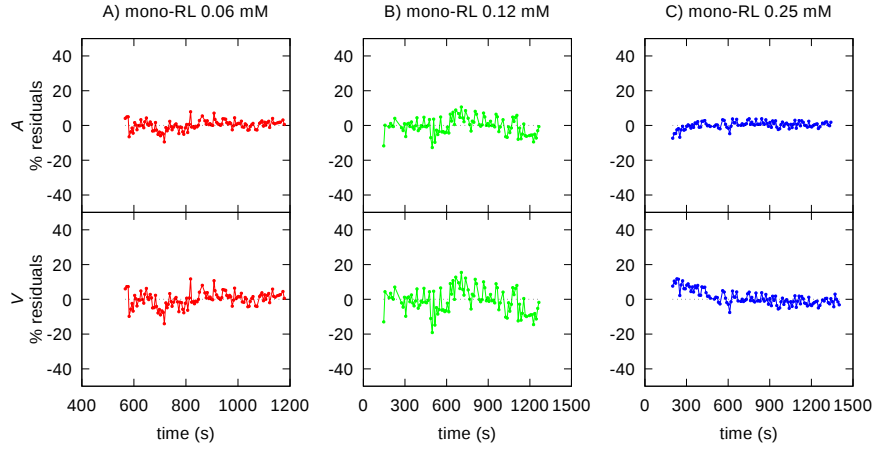


Figure S14: Residuals plots of fitting curves shown in Fig. S13.

		mono-RL 0.06 mM	mono-RL 0.12 mM	mono-RL 0.25 mM
		A	B	C
N	(10^9)	4.41 ± 0.04	0.924 ± 0.009	3.84 ± 0.04
V_0	$(10^4 \mu\text{m}^3)$	0.781 ± 0.009	0.122 ± 0.005	1.0 ± 0.2
λ_1	(μm)	2.86 ± 0.05	2.88 ± 0.05	5.6 ± 0.4
λ_2	(μm)	17 ± 3	29 ± 1	29.8 ± 0.6
r_p	(\AA)	2.8 ± 0.1	3.8 ± 0.2	4.5 ± 0.1
m		1.27 ± 0.01	1.05 ± 0.03	1.36 ± 0.01
n		9.9 ± 0.1	7.2 ± 0.4	1.25 ± 0.08
pk_{1+}	$(k_{1+} \text{ in } s^{-1}M^{-m})$	-2.60 ± 0.03	-2.05 ± 0.06	-2.27 ± 0.02
pk_{1-}	$(k_{1-} \text{ in } s^{-1})$	4.61 ± 0.05	4.99 ± 0.08	5.73 ± 0.06
pk_{2+}	$(k_{2+} \text{ in } s^{-1}M^{1-n})$	-92 ± 5	72 ± 3	28 ± 2
pk_{2-}	$(k_{2-} \text{ in } s^{-1})$	224 ± 6	148 ± 4	32.5 ± 0.9

Table S4: Parameters obtained by the simultaneous best fit of areas and volumes of the DOPC:SM:CHOL 1:1:1 GUVs (experiment n. 2, Figs. S10, S11 and S17) in the presence of mono-RL shown as solid black lines in Fig. S13.

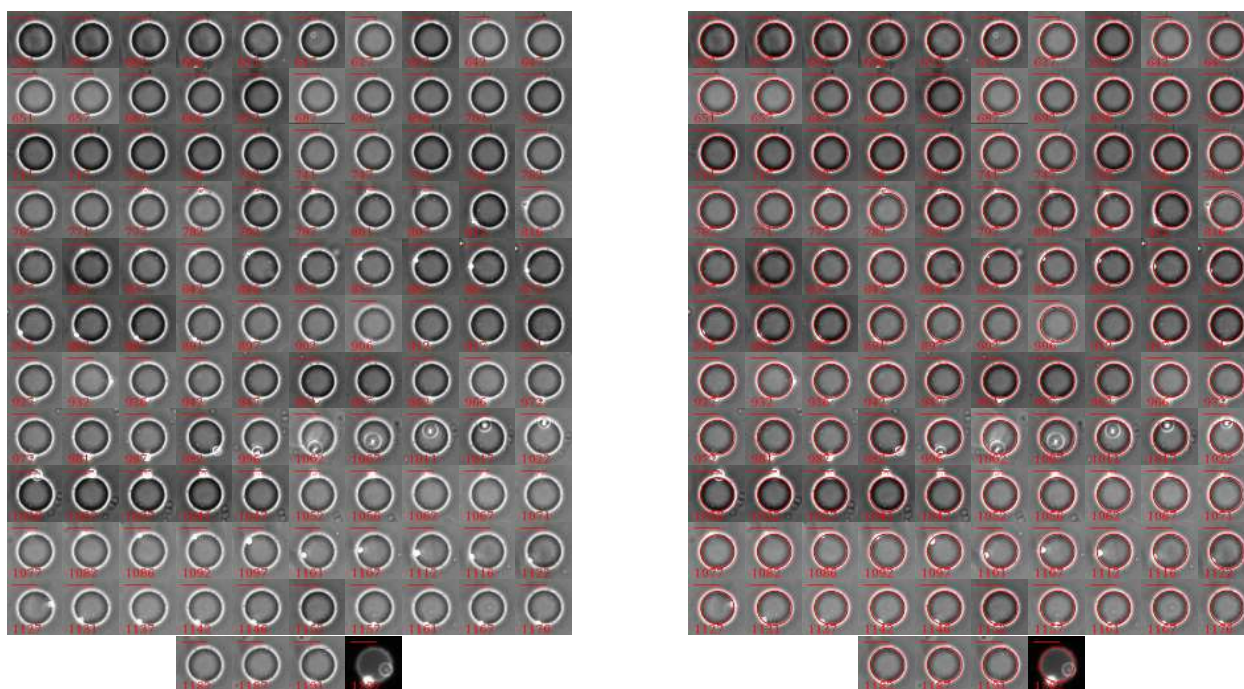


Figure S15: Microscope images (left) and best fit contours (right) of a selected DOPC:SM:CHOL 1:1:1 GUV (experiment n. 3) in the presence of 0.06 mM mono-RL.

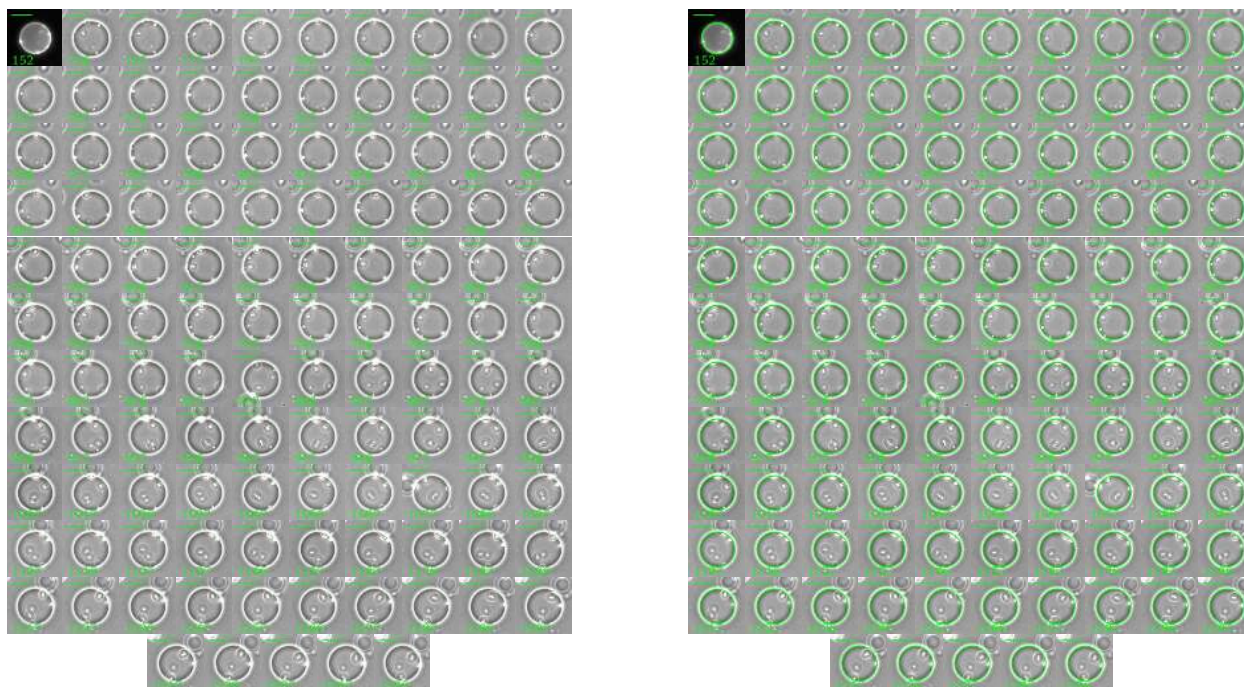


Figure S16: Microscope images (left) and best fit contours (right) of a selected DOPC:SM:CHOL 1:1:1 GUV (experiment n. 3) in the presence of 0.12 mM mono-RL.

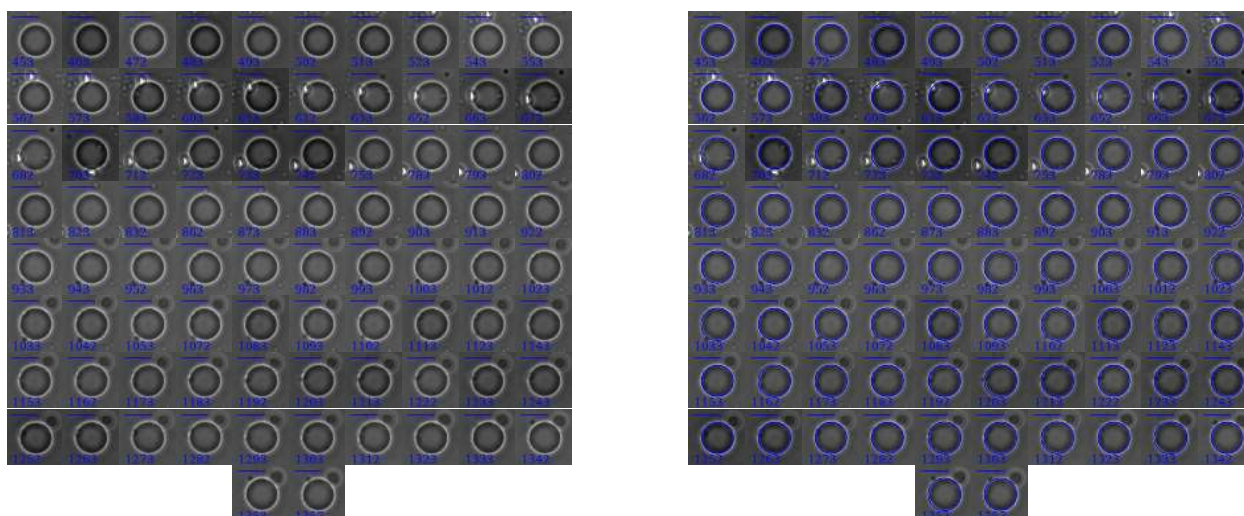


Figure S17: Microscope images (left) and best fit contours (right) of a selected DOPC:SM:CHOL 1:1:1 GUV (experiment n. 3) in the presence of 0.25 mM mono-RL.

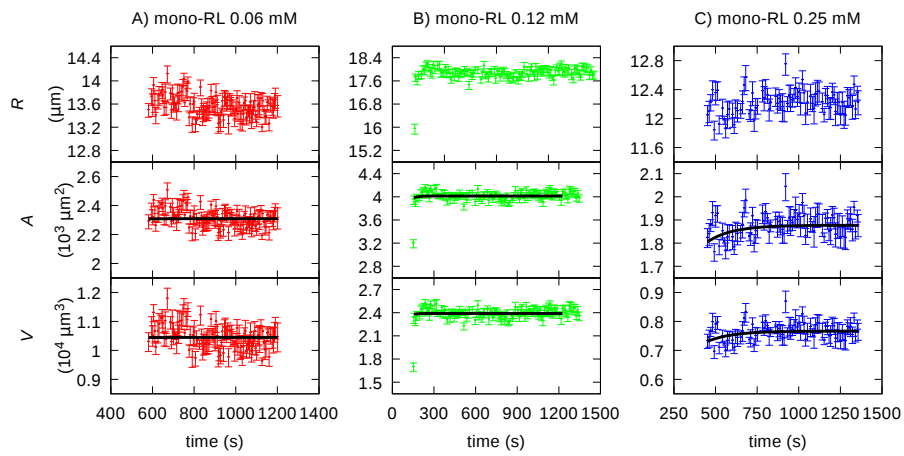


Figure S18: Time-dependence of the geometrical parameters of the DOPC:SM:CHOL (1:1:1) GUVs (experiment n. 3, Figs. S15, S16 and S17) in the presence of 0.06 mM, 0.12 mM and 0.25 mM (red, green and blue circles respectively) mono-RL (panel A, B and C). Panels A to C: the top plot corresponds to GUVs average radius, the second one to the GUV area, the third one to the GUV volume. Solid black lines are the best fit of area and volume obtained with Eq. 18 and 21, respectively. Residual plots are shown in Fig. S19.

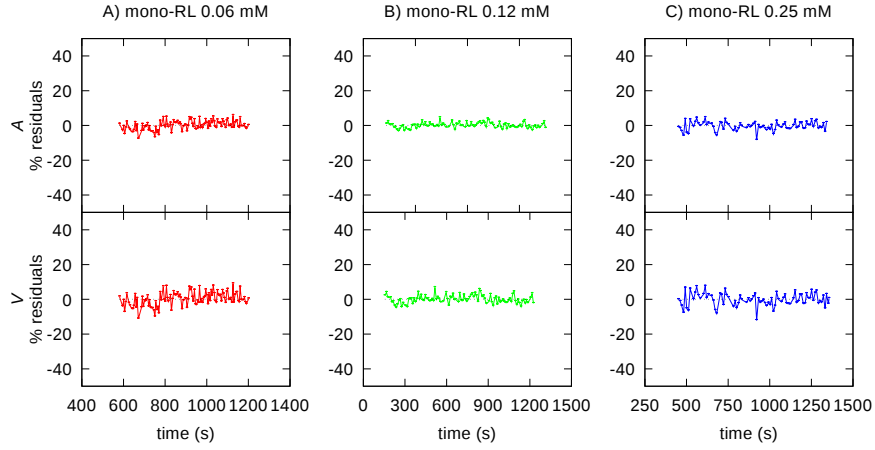


Figure S19: Residuals plots of fitting curves shown in Fig. S18.

		mono-RL 0.06 mM	mono-RL 0.12 mM	mono-RL 0.25 mM
		A	B	C
N	(10^9)	2.79 ± 0.05	3.46 ± 0.05	1.63 ± 0.06
V_0	$(10^4 \mu\text{m}^3)$	0.562 ± 0.007	1.47 ± 0.02	0.020 ± 0.006
λ_1	(μm)	2.88 ± 0.03	2.86 ± 0.06	4.95 ± 0.05
λ_2	(μm)	17 ± 3	28 ± 1	29.5 ± 0.6
r_p	(\AA)	2.8 ± 0.1	3.8 ± 0.2	4.5 ± 0.1
m		1.29 ± 0.02	1.00 ± 0.02	1.05 ± 0.07
n		9.7 ± 0.1	7.2 ± 0.4	1.25 ± 0.07
pk_{1+}	$(k_{1+} \text{ in } \text{s}^{-1}\text{M}^{-m})$	-2.88 ± 0.04	-2.07 ± 0.05	-1.2 ± 0.1
pk_{1-}	$(k_{1-} \text{ in } \text{s}^{-1})$	4.72 ± 0.05	4.14 ± 0.04	5.6 ± 0.2
pk_{2+}	$(k_{2+} \text{ in } \text{s}^{-1}\text{M}^{1-n})$	-92 ± 5	70 ± 2	22 ± 2
pk_{2-}	$(k_{2-} \text{ in } \text{s}^{-1})$	218 ± 6	138 ± 4	26 ± 1

Table S5: Parameters obtained by the simultaneous best fit of areas and volumes of the DOPC:SM:CHOL 1:1:1 GUVs (experiment n. 3, Figs. S15, S16 and S17) in the presence of mono-RL shown as solid black lines in Fig. S18.

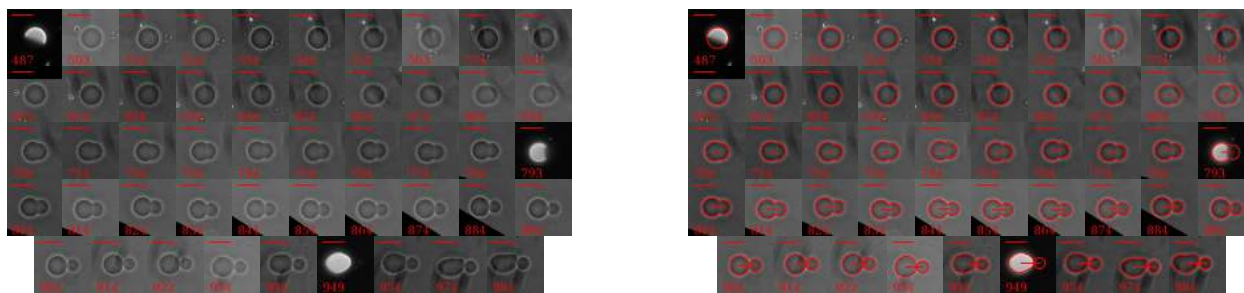


Figure S20: Microscope images (left) and best fit contours (right) of a selected DOPC:SM:CHOL 1:1:1 GUV (experiment n. 1) in the presence of 0.06 mM di-RL.

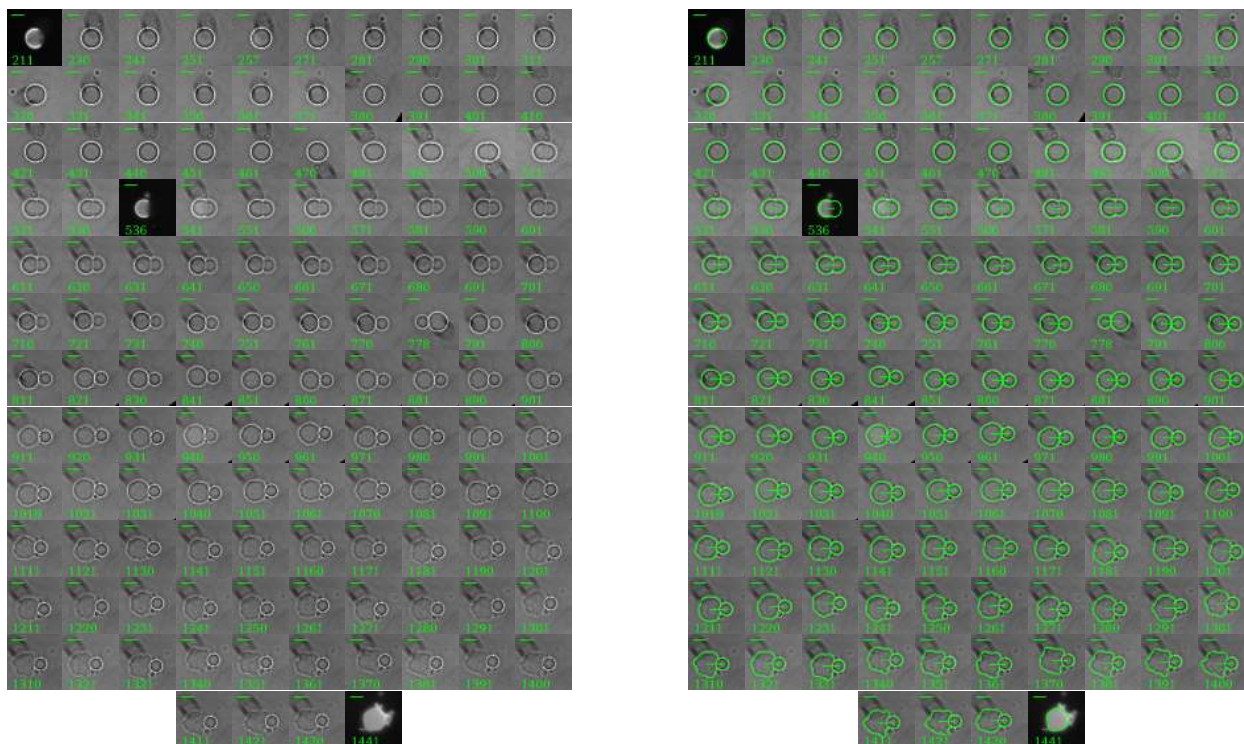


Figure S21: Microscope images (left) and best fit contours (right) of a selected DOPC:SM:CHOL 1:1:1 GUV (experiment n. 1) in the presence of 0.12 mM di-RL.

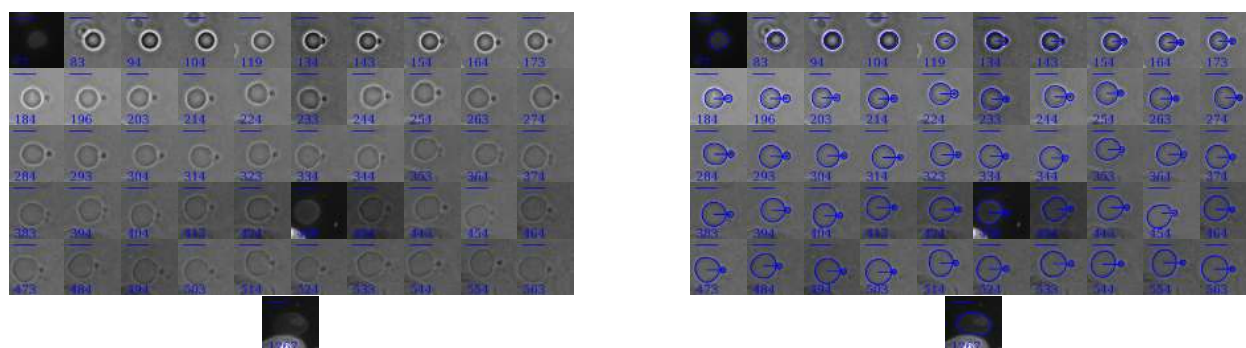


Figure S22: Microscope images (left) and best fit contours (right) of a selected DOPC:SM:CHOL 1:1:1 GUV (experiment n. 1) in the presence of 0.25 mM di-RL.

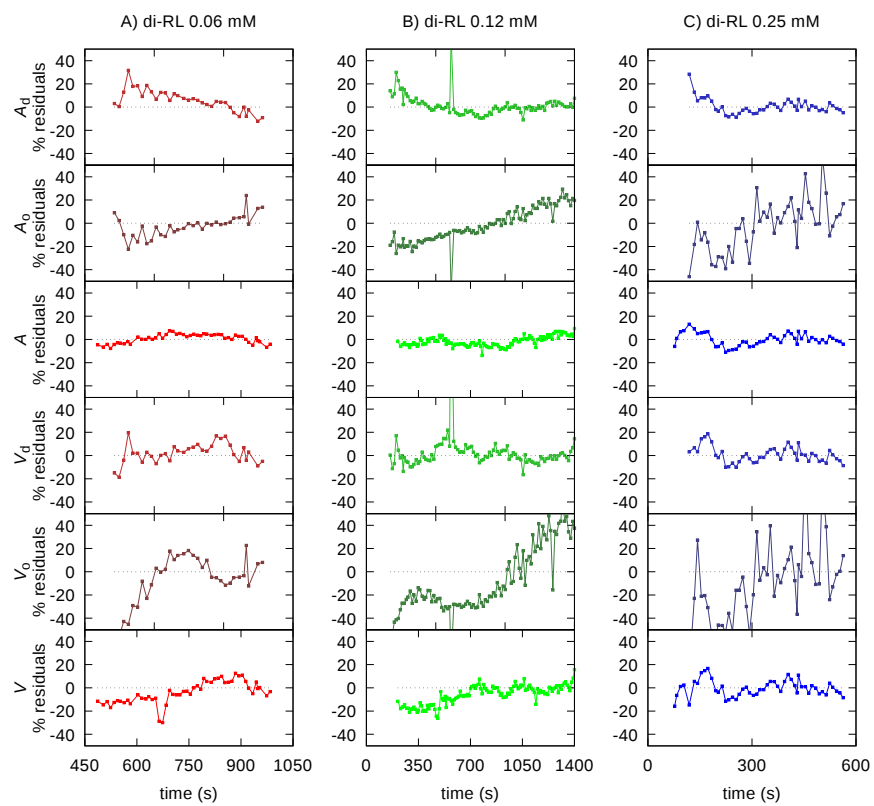


Figure S23: Residuals plots of fitting curves shown in Fig. 7.

		di-RL 0.06 mM	di-RL 0.12 mM	di-RL 0.25 mM
		A	B	C
N_d	(10^9)	1.90 ± 0.04	5.67 ± 0.08	2.0 ± 0.1
$V_{d,0}$	($10^4 \mu\text{m}^3$)	0.273 ± 0.007	1.27 ± 0.01	0.183 ± 0.005
$\lambda_{d,1}$	(μm)	0.109 ± 0.005	0.087 ± 0.004	0.087 ± 0.004
$\lambda_{d,2}$	(μm)	3.1 ± 0.6	8.75 ± 0.09	6.5 ± 0.1
$r_{d,p}$	(\AA)	500 ± 5	489 ± 5	500 ± 5
m_d		1.06 ± 0.01	1.04 ± 0.01	1.00 ± 0.01
n_d		3.45 ± 0.03	4.21 ± 0.04	1.27 ± 0.01
pk_{d1+}	(k_{d1+} in $\text{s}^{-1}\text{M}^{-m_d}$)	-0.243 ± 0.005	0.060 ± 0.003	-0.2 ± 0.1
pk_{d1-}	(k_{d1-} in s^{-1})	10.6 ± 0.1	11.1 ± 0.1	6.00 ± 0.06
pk_{d2+}	(k_{d2+} in $\text{s}^{-1}\text{M}^{1-n_d}$)	-32.0 ± 0.3	-43.7 ± 0.4	2.12 ± 0.06
pk_{d2-}	(k_{d2-} in s^{-1})	38.0 ± 0.5	40.8 ± 0.6	6.12 ± 0.06
N_o	(10^9)	2.27 ± 0.02	7.36 ± 0.07	0.517 ± 0.005
$V_{o,0}$	($10^4 \mu\text{m}^3$)	0.059 ± 0.003	0.359 ± 0.004	0.0061 ± 0.0007
$\lambda_{o,1}$	(μm)	10.4 ± 0.1	8.5 ± 0.3	8.3 ± 0.2
$\lambda_{o,2}$	(μm)	29.9 ± 0.4	30.0 ± 0.5	29.5 ± 0.4
$r_{o,p}$	(\AA)	500 ± 5	480 ± 10	480 ± 10
m_o		1.08 ± 0.03	1.60 ± 0.05	1.1 ± 0.1
n_o		7.25 ± 0.08	7.3 ± 0.2	7.3 ± 0.2
pk_{o1+}	(k_{o1+} in $\text{s}^{-1}\text{M}^{-m_o}$)	0.189 ± 0.008	0.30 ± 0.01	0.19 ± 0.03
pk_{o1-}	(k_{o1-} in s^{-1})	5.0 ± 0.1	4.02 ± 0.09	3.1 ± 0.2
pk_{o2+}	(k_{o2+} in $\text{s}^{-1}\text{M}^{1-n_o}$)	69 ± 1	124 ± 3	83 ± 5
pk_{o2-}	(k_{o2-} in s^{-1})	62 ± 2	93 ± 3	64 ± 4

Table S6: Parameters obtained by the simultaneous best fit of areas and volumes of the DOPC:SM:CHOL 1:1:1 GUVs (experiment n. 1, Figs. S20, S21 and S22) in the presence of di-RL shown as solid black lines in Fig. 7.

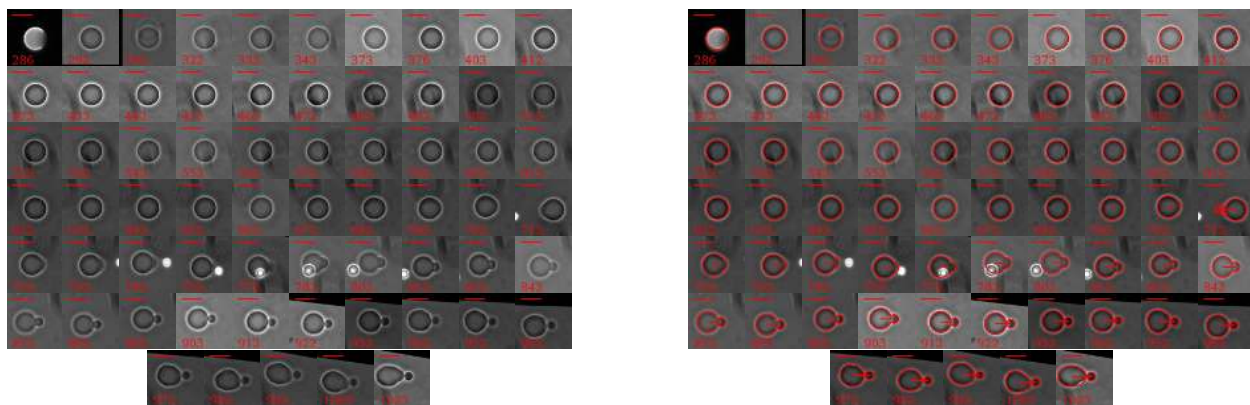


Figure S24: Microscope images (left) and best fit contours (right) of a selected DOPC:SM:CHOL 1:1:1 GUV (experiment n. 2) in the presence of 0.06 mM di-RL.

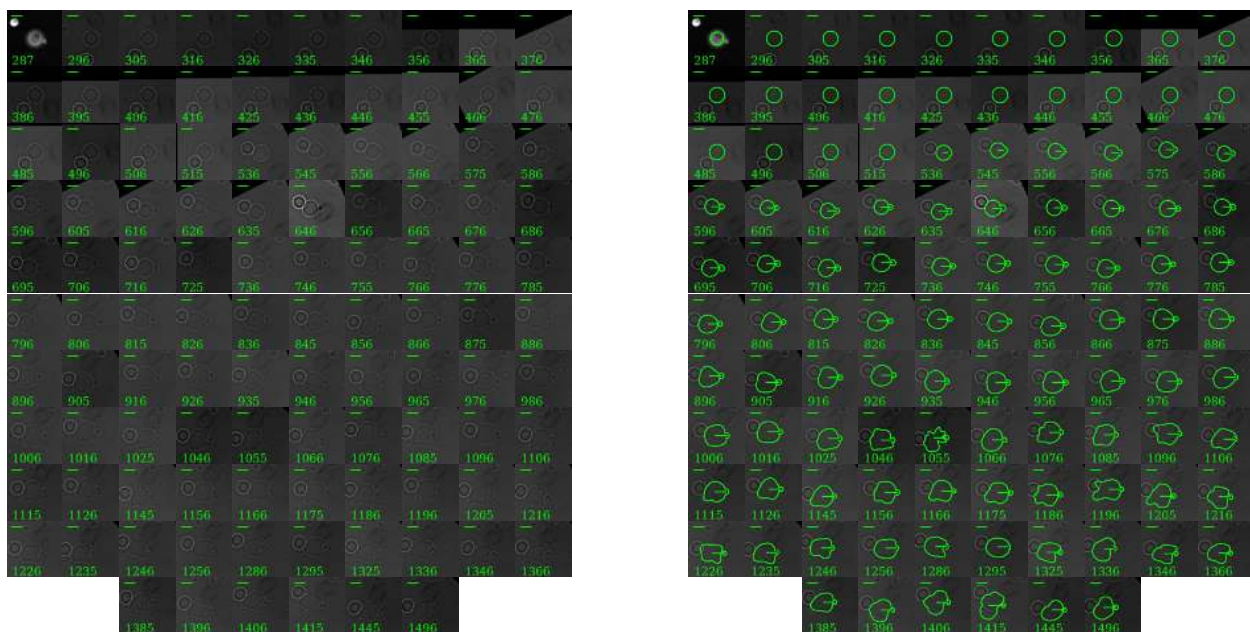


Figure S25: Microscope images (left) and best fit contours (right) of a selected DOPC:SM:CHOL 1:1:1 GUV (experiment n. 2) in the presence of 0.12 mM di-RL.

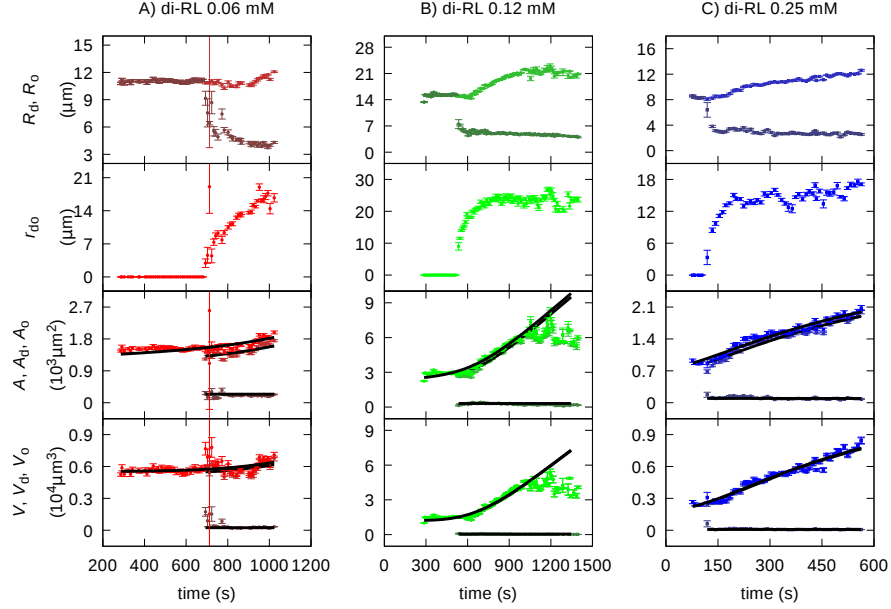


Figure S26: Time-dependence of the geometrical parameters of the DOPC:SM:CHOL (1:1:1) GUVs (experiment n. 2, Figs. S24, S25 and S22) in the presence of 0.06 mM, 0.12 mM and 0.25 mM (red, green and blue circles respectively) di-RL (panel A, B and C). Panels A to C: the top plot corresponds to the average radius of the GUV L_d phase (intermediate-shade colors) and L_o phase (dark-shade colors); the second plot reports the distance between the center of the L_d phase and the one of the L_o phase; the third plot reports the L_d phase GUV area (intermediate shade color) and the best fit obtained with Eq. 27 (with $\alpha = d$, solid black lines), the L_o phase GUV area (dark-shade color) and the best fit obtained with Eq. 27 (with $\alpha = o$, solid black lines), and the total GUV area with the best fit obtained with Eq. 27 (by the sum for $\alpha = d, o$, solid black line); the fourth plot reports the L_d phase GUV volume (intermediate shade color) and the best fit obtained with Eq. 28 (with $\alpha = d$, solid black lines), the L_o phase GUV volume (dark-shade color) and the best fit obtained with Eq. 28 (with $\alpha = o$, solid black lines), and the total GUV volume with the best fit obtained with Eq. 28 (by the sum for $\alpha = d, o$, solid black line). Residual plots are shown in Fig. S27.

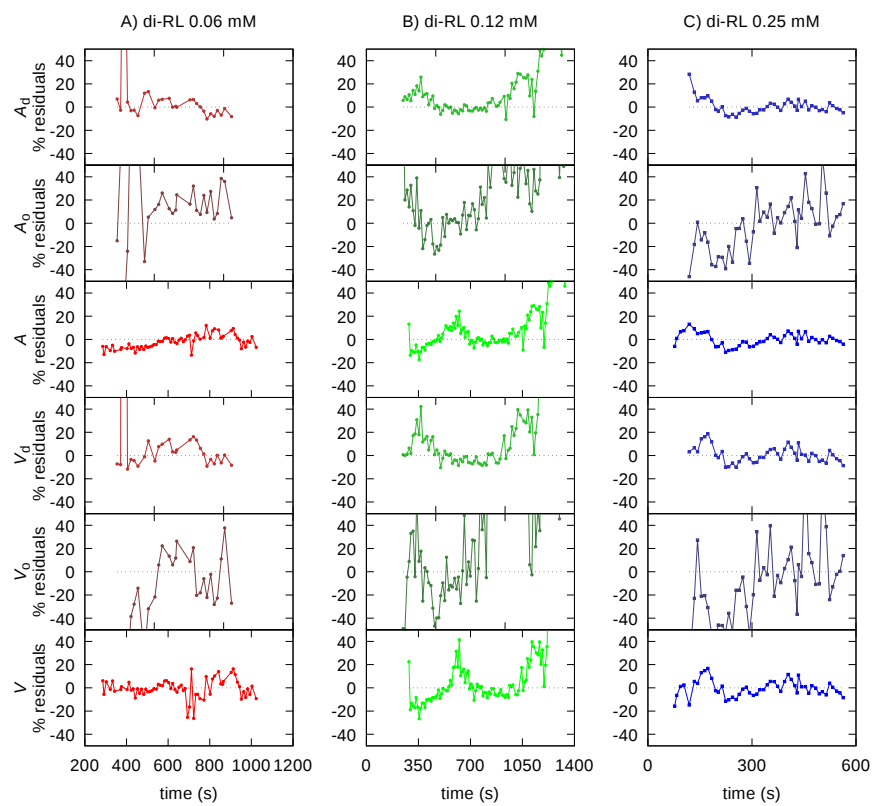


Figure S27: Residuals plots of fitting curves shown in Fig. S26.

		di-RL 0.06 mM	di-RL 0.12 mM	di-RL 0.25 mM
		A	B	C
N_d	(10^9)	3.22 ± 0.05	5.86 ± 0.06	2.0 ± 0.1
$V_{d,0}$	($10^4 \mu\text{m}^3$)	0.531 ± 0.005	1.16 ± 0.02	0.183 ± 0.005
$\lambda_{d,1}$	(μm)	0.109 ± 0.005	0.087 ± 0.004	0.087 ± 0.004
$\lambda_{d,2}$	(μm)	3.2 ± 0.6	8.95 ± 0.09	6.5 ± 0.1
$r_{d,p}$	(\AA)	500 ± 5	500 ± 5	500 ± 5
m_d		1.08 ± 0.01	1.00 ± 0.01	1.00 ± 0.01
n_d		3.49 ± 0.03	3.98 ± 0.04	1.27 ± 0.01
pk_{d1+}	(k_{d1+} in $\text{s}^{-1}\text{M}^{-m_d}$)	-0.245 ± 0.005	0.058 ± 0.002	-0.2 ± 0.1
pk_{d1-}	(k_{d1-} in s^{-1})	10.8 ± 0.1	10.8 ± 0.1	6.00 ± 0.06
pk_{d2+}	(k_{d2+} in $\text{s}^{-1}\text{M}^{1-n_d}$)	-31.7 ± 0.3	-39.8 ± 0.4	2.12 ± 0.06
pk_{d2-}	(k_{d2-} in s^{-1})	39.0 ± 0.5	37.3 ± 0.5	6.12 ± 0.06
N_o	(10^9)	1.30 ± 0.02	1.73 ± 0.02	0.517 ± 0.005
$V_{o,0}$	($10^4 \mu\text{m}^3$)	0.017 ± 0.002	0.0435 ± 0.0004	0.0061 ± 0.0007
$\lambda_{o,1}$	(μm)	10.4 ± 0.1	8.5 ± 0.3	8.3 ± 0.2
$\lambda_{o,2}$	(μm)	29.9 ± 0.4	30.0 ± 0.5	29.5 ± 0.4
$r_{o,p}$	(\AA)	500 ± 5	480 ± 10	480 ± 10
m_o		1.08 ± 0.03	1.60 ± 0.05	1.1 ± 0.1
n_o		7.26 ± 0.08	7.3 ± 0.2	7.3 ± 0.2
pk_{o1+}	(k_{o1+} in $\text{s}^{-1}\text{M}^{-m_o}$)	0.189 ± 0.007	0.30 ± 0.01	0.19 ± 0.03
pk_{o1-}	(k_{o1-} in s^{-1})	5.0 ± 0.1	4.00 ± 0.09	3.1 ± 0.2
pk_{o2+}	(k_{o2+} in $\text{s}^{-1}\text{M}^{1-n_o}$)	69 ± 1	124 ± 3	83 ± 5
pk_{o2-}	(k_{o2-} in s^{-1})	63 ± 2	93 ± 3	64 ± 4

Table S7: Parameters obtained by the simultaneous best fit of areas and volumes of the DOPC:SM:CHOL 1:1:1 GUVs (experiment n. 2, Figs. S24, S25 and S22) in the presence of di-RL shown as solid black lines in Fig. S26. The C column reports the value of the experiment n. 1.

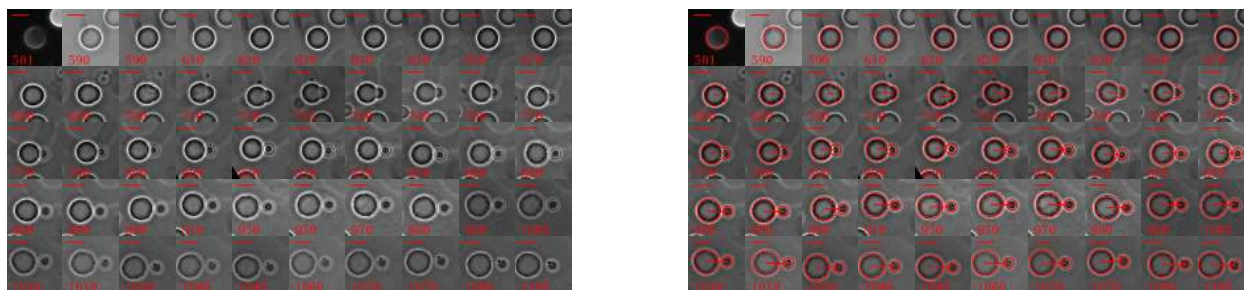


Figure S28: Microscope images (left) and best fit contours (right) of a selected DOPC:SM:CHOL 1:1:1 GUV (experiment n. 3) in the presence of 0.06 mM di-RL.



Figure S29: Microscope images (left) and best fit contours (right) of a selected DOPC:SM:CHOL 1:1:1 GUV (experiment n. 3) in the presence of 0.12 mM di-RL.

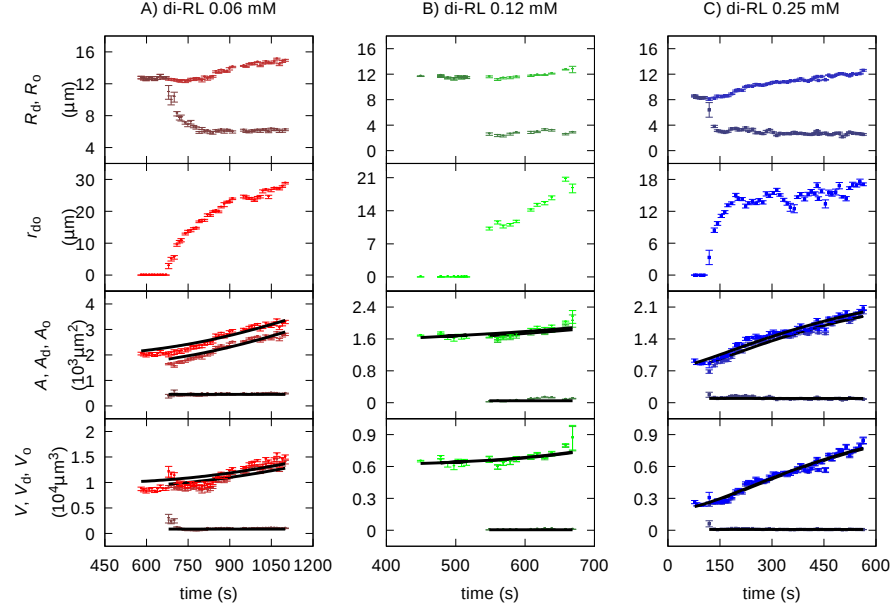


Figure S30: Time-dependence of the geometrical parameters of the DOPC:SM:CHOL (1:1:1) GUVs (experiment n. 3, Figs. S28, S29 and S22) in the presence of 0.06 mM, 0.12 mM and 0.25 mM (red, green and blue circles respectively) di-RL (panel A, B and C). Panels A to C: the top plot corresponds to the average radius of the GUV L_d phase (intermediate-shade colors) and L_o phase (dark-shade colors); the second plot reports the distance between the center of the L_d phase and the one of the L_o phase; the third plot reports the L_d phase GUV area (intermediate shade color) and the best fit obtained with Eq. 27 (with $\alpha = d$, solid black lines), the L_o phase GUV area (dark-shade color) and the best fit obtained with Eq. 27 (with $\alpha = o$, solid black lines), and the total GUV area with the best fit obtained with Eq. 27 (by the sum for $\alpha = d, o$, solid black line); the fourth plot reports the L_d phase GUV volume (intermediate shade color) and the best fit obtained with Eq. 28 (with $\alpha = d$, solid black lines), the L_o phase GUV volume (dark-shade color) and the best fit obtained with Eq. 28 (with $\alpha = o$, solid black lines), and the total GUV volume with the best fit obtained with Eq. 28 (by the sum for $\alpha = d, o$, solid black line). Residual plots are shown in Fig. S31.

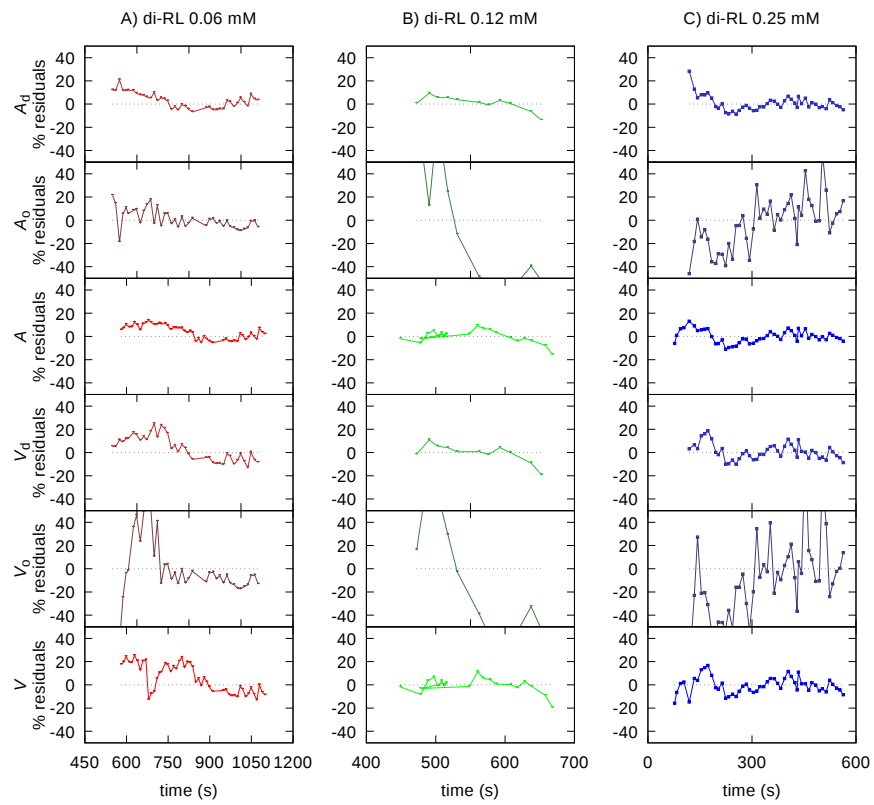


Figure S31: Residuals plots of fitting curves shown in Fig. S30.

		di-RL 0.06 mM	di-RL 0.12 mM	di-RL 0.25 mM
		A	B	C
N_d	(10^9)	4.1 ± 0.2	3.98 ± 0.05	2.0 ± 0.1
$V_{d,0}$	($10^4 \mu\text{m}^3$)	0.89 ± 0.08	0.604 ± 0.008	0.183 ± 0.005
$\lambda_{d,1}$	(μm)	0.108 ± 0.005	0.087 ± 0.004	0.087 ± 0.004
$\lambda_{d,2}$	(μm)	3.2 ± 0.6	8.83 ± 0.09	6.5 ± 0.1
$r_{d,p}$	(\AA)	500 ± 5	494 ± 5	500 ± 5
m_d		1.07 ± 0.01	1.03 ± 0.01	1.00 ± 0.01
n_d		3.37 ± 0.03	4.16 ± 0.04	1.27 ± 0.01
pk_{d1+}	(k_{d1+} in $\text{s}^{-1}\text{M}^{-m_d}$)	-0.245 ± 0.005	0.060 ± 0.003	-0.2 ± 0.1
pk_{d1-}	(k_{d1-} in s^{-1})	10.7 ± 0.1	11.0 ± 0.1	6.00 ± 0.06
pk_{d2+}	(k_{d2+} in $\text{s}^{-1}\text{M}^{1-n_d}$)	-31.0 ± 0.3	-42.0 ± 0.4	2.12 ± 0.06
pk_{d2-}	(k_{d2-} in s^{-1})	37.6 ± 0.4	40.0 ± 0.6	6.12 ± 0.06
N_o	(10^9)	2.46 ± 0.03	0.277 ± 0.004	0.517 ± 0.005
$V_{o,0}$	($10^4 \mu\text{m}^3$)	0.073 ± 0.004	0.0047 ± 0.0001	0.0061 ± 0.0007
$\lambda_{o,1}$	(μm)	10.4 ± 0.1	8.5 ± 0.3	8.3 ± 0.2
$\lambda_{o,2}$	(μm)	29.9 ± 0.4	30.0 ± 0.5	29.5 ± 0.4
$r_{o,p}$	(\AA)	500 ± 5	480 ± 10	480 ± 10
m_o		1.08 ± 0.03	1.60 ± 0.05	1.1 ± 0.1
n_o		7.27 ± 0.08	7.3 ± 0.2	7.3 ± 0.2
pk_{o1+}	(k_{o1+} in $\text{s}^{-1}\text{M}^{-m_o}$)	0.188 ± 0.007	0.30 ± 0.01	0.19 ± 0.03
pk_{o1-}	(k_{o1-} in s^{-1})	5.0 ± 0.1	4.01 ± 0.09	3.1 ± 0.2
pk_{o2+}	(k_{o2+} in $\text{s}^{-1}\text{M}^{1-n_o}$)	69 ± 1	124 ± 3	83 ± 5
pk_{o2-}	(k_{o2-} in s^{-1})	63 ± 2	93 ± 3	64 ± 4

Table S8: Parameters obtained by the simultaneous best fit of areas and volumes of the DOPC:SM:CHOL 1:1:1 GUVs (experiment n. 3, Figs. S28, S29 and S22) in the presence of di-RL shown as solid black lines in Fig. S30. The C column reports the value of the experiment n. 1.

References

- [1] Come, B.; Donato, M.; Potenza, L. F.; Mariani, P.; Itri, R.; Spinozzi, F. The intriguing role of rhamnolipids on plasma membrane remodelling: From lipid rafts to membrane budding. *Journal of Colloid and Interface Science* **2021**, *582*, 669–677.